



**HAL**  
open science

## From behavior to circuit modeling of light-seeking navigation in zebrafish larvae

Sophia Karpenko, Sébastien Wolf, Julie Lafaye, Guillaume Le Goc, Volker Bormuth, Raphaël Candelier, Georges Debrégeas

► **To cite this version:**

Sophia Karpenko, Sébastien Wolf, Julie Lafaye, Guillaume Le Goc, Volker Bormuth, et al.. From behavior to circuit modeling of light-seeking navigation in zebrafish larvae. 2019. hal-02413703

**HAL Id: hal-02413703**

**<https://hal.science/hal-02413703>**

Preprint submitted on 16 Dec 2019

**HAL** is a multi-disciplinary open access archive for the deposit and dissemination of scientific research documents, whether they are published or not. The documents may come from teaching and research institutions in France or abroad, or from public or private research centers.

L'archive ouverte pluridisciplinaire **HAL**, est destinée au dépôt et à la diffusion de documents scientifiques de niveau recherche, publiés ou non, émanant des établissements d'enseignement et de recherche français ou étrangers, des laboratoires publics ou privés.

# 1 From behavior to circuit modeling of 2 light-seeking navigation in zebrafish 3 larvae

4 **Sophia Karpenko<sup>1,2</sup>, Sébastien Wolf<sup>3,4</sup>, Julie Lafaye<sup>1</sup>, Guillaume Le Goc<sup>1</sup>, Thomas  
5 Panier<sup>1</sup>, Volker Bormuth<sup>1</sup>, Raphaël Candelier<sup>1</sup>, Georges Debrégeas<sup>1\*</sup>**

\*For correspondence:

[georges.debregeas@upmc.fr](mailto:georges.debregeas@upmc.fr) (LJP)

6 <sup>1</sup>Sorbonne Université, CNRS, Institut de Biologie Paris-Seine (IBPS), Laboratoire Jean  
7 Perrin (LJP), F-75005, Paris; <sup>2</sup>Paris Sciences & Lettres, 60 rue Mazarine, F-75006 Paris,  
8 France; <sup>3</sup>Laboratoire de Physique de l'Ecole Normale Supérieure, CNRS UMR 8023 & PSL  
9 Research, Paris, France; <sup>4</sup>Institut de Biologie de l'Ecole Normale Supérieure, CNRS,  
10 INSERM, UMR 8197 & PSL Research, Paris, France

---

## 12 Abstract

13 Bridging brain-scale circuit dynamics and organism-scale behavior is a central challenge in  
14 neuroscience. It requires the concurrent development of minimal behavioral and neural circuit  
15 models that can quantitatively capture basic sensorimotor operations. Here we focus on  
16 light-seeking navigation in zebrafish larvae. Using a virtual reality assay, we first characterize how  
17 motor and visual stimulation sequences govern the selection of discrete swim-bout events that  
18 subserve the fish navigation in the presence of a distant light source. These mechanisms are  
19 combined into a comprehensive Markov-chain model of navigation that quantitatively predict the  
20 stationary distribution of the fish's body orientation under any given illumination profile. We then  
21 map this behavioral description onto a neuronal model of the ARTR, a small neural circuit involved  
22 in the orientation-selection of swim bouts. We demonstrate that this visually-biased  
23 decision-making circuit can similarly capture the statistics of both spontaneous and contrast-driven  
24 navigation.

---

## 26 Introduction

27 Animal behaviors are both stereotyped and variable: they are constrained at short time scale to a  
28 finite motor repertoire while the long-term sequence of successive motor actions displays apparent  
29 stochasticity. Behavior is thus best described as a set of statistic rules that defines how elementary  
30 motor actions are chained. In the presence of sensory cues, two types of behavioral responses can  
31 be distinguished. If they signal an immediate threat or reward (e.g. the presence of a predator or  
32 a prey), they may elicit a discrete behavioral switch as the animal engages in a specialized motor  
33 program (e.g. escape or hunt, *Budick and O'Malley (2000)*; *Fiser et al. (2004)*; *Bianco et al. (2011)*;  
34 *McClenahan et al. (2012)*; *Bianco and Engert (2015)*). However, most of the time, sensory cues  
35 merely reflect changes in external factors as the animal navigates through a complex environment.  
36 These weak motor-related cues interfere with the innate motor program to cumulatively promote  
37 the exploration of regions that are more favorable for the animal (*Tsodyks et al., 1999*; *Fiser et al.,*  
38 *2004*).

39 A quantification of sensory-biased locomotion thus requires to first categorize the possible  
40 movements, and then to evaluate the statistical rules that relate the selection of these different

41 actions to the sensory and motor history. Although the probabilistic nature of these rules generally  
42 precludes a deterministic prediction of the animal's trajectory, they may still provide a quantification  
43 of the probability distribution of presence within a given environment after a given exploration  
44 time.

45 In physics terms, the animal can thus be described as a random walker, whose transition  
46 probabilities are a function of the sensory inputs. This statistical approach was originally introduced  
47 to analyze bacteria chemotaxis (*Lovely and Dahlquist, 1975*). Motile bacteria navigate by alternating  
48 straight swimming and turning phases, so-called runs and tumbles, resulting in trajectories akin to  
49 random walks (*Berg and Brown, 1972*). Chemotaxis originates from a chemical-driven modulation  
50 of the transition probability from run to tumble: the transition rate is governed by the time-history  
51 of chemical sensing. How this dependency is optimized to enhance gradient-climbing has been  
52 the subject of extensive literature (*Macnab and Koshland, 1972; Adler and Tso, 1974; Mello and*  
53 *Tu, 2007; Yuan et al., 2010; Celani and Vergassola, 2010*). More recently, similar descriptions have  
54 been successfully used to quantify chemotaxis and phototaxis in multi-cellular organisms such as *C.*  
55 *elegans* (*Ward, 1973; Miller et al., 2005; Ward et al., 2008*), *Drosophila* larva (*Sawin et al., 1994; Kane*  
56 *et al., 2013; Gomez-Marin et al., 2011; Tastekin et al., 2018*) or different types of slugs (*Matsuo*  
57 *et al., 2014; Marée et al., 1999*). Although the sensorimotor apparatus of these animals are very  
58 different, the taxis strategies at play appear to be convergent and can be classified based on the  
59 gradient sensing methods (*Fraenkel and Gunn, 1961; Gomez-Marin and Louis, 2012*). Tropotaxis  
60 refers to strategies in which the organism directly and instantaneously infers the stimulus direction  
61 by comparison between two spatially distinct sensory receptors. In contrast, during klinotaxis, the  
62 sensory gradient is inferred from successive samplings at different spatial positions. This second  
63 strategy is particularly adapted when the organism has only one receptor, or if the sensory gradient  
64 across the animal's body is too small to be detected (*Humberg et al., 2018*). It requires at least a  
65 basic form of memory, since the sensory information needs to be retained for some finite period of  
66 time.

67 In the present work, we implement such a framework to produce a comprehensive statistical  
68 model of phototaxis in zebrafish larvae. Zebrafish larva is currently the only vertebrate system  
69 that allows *in vivo* whole-brain functional imaging at cellular resolution (*Panier et al., 2013; Ahrens*  
70 *et al., 2013*). It thus provides a unique opportunity to study how sensorimotor tasks, such as  
71 sensory-driven locomotion, are implemented at the brain-scale level.

72 Although adult zebrafish are generally photophobic (or scototactic, *Serra et al. (1999); Maximino*  
73 *et al. (2007)*), they display positive phototaxis at the larval stage, from 5 days post-fertilization (dpf)  
74 on (*Orger and Baier, 2005*). At this early stage, their locomotion consists of a series of discrete  
75 swimming events interspersed by  $\sim 1$  s long periods of inactivity (*Girdhar et al., 2015*). Previous  
76 studies have shown that, when exposed to a distant light source, the first bout executed by  
77 the fish tend to be orientated in the direction of the source (tropotaxis) (*Burgess et al., 2010*).  
78 Furthermore, *Chen and Engert (2014)* have shown, using a virtual reality assay, that zebrafish  
79 are able to confine their navigation within a bright region within a dark environment even when  
80 deprived from stereovisual contrast information. This latter study thus established that their  
81 phototactic behavior also involves a spatio-temporal integration mechanism (klinotaxis).

82 From a neuronal viewpoint, recent calcium imaging experiments identified a well defined circuit  
83 in the rostral hindbrain that plays a key role in phototaxis (*Ahrens et al., 2013; Dunn et al., 2016;*  
84 *Wolf et al., 2017*). This region, called ARTR (anterior rhombencephalic turning region) or HBO  
85 (hindbrain oscillator), displays pseudo-periodic antiphase oscillations, such that the activity of the  
86 left and right subpopulations alternate with a  $\sim 20$ s period. This alternation was shown to set the  
87 coordinated direction of the gaze and tail bout orientation, thus effectively organizing the temporal  
88 sequence of the successive reorientations. It was further shown that this circuit oscillation could be  
89 driven by whole-field illumination of the ipsilateral eye, such as to favor the animal's orientation  
90 towards a light source (*Wolf et al., 2017*).

91 In the present study, we aim at quantifying the statistical rules that control the larva's reorien-

92 tation dynamics in the presence of a continuous angular gradient of illumination (orientational  
93 phototaxis). Using a virtual-reality closed-loop assay, we quantify how swim bouts selection is  
94 statistically controlled by the light intensity received on both eyes prior to the bout initiation, or  
95 the change in illumination elicited by the previous swim bout. Our experimental configuration  
96 allows us to disentangle the contribution of the two aforementioned strategies: tropotaxis and  
97 klinotaxis. From the analysis of this short-term behavior, we built a minimal Markov model of  
98 phototaxis, from which we compute the long-term distribution of orientations for any angular  
99 profile of illumination. This model offers explicit predictions of the statistics of the fish orientation  
100 that quantitatively compare with the experimental observations. We further expand on a recent  
101 rate model of the ARTR circuit to propose a functional neuronal model of spontaneous navigation  
102 and contrast-biased orientation selection. We demonstrate that the statistics of turn orientation  
103 can be fully understood by assuming that this self-oscillating circuitry, that selects the orientation of  
104 turning bouts, integrates stereovisual contrast in the form of incoming currents proportional to the  
105 visual stimulus.

## 106 Results

### 107 Kinematics of spontaneous navigation as a first-order autoregressive process

108 Zebrafish larvae aged 5-7 dpf were placed one at a time in a Petri dish (14cm in diameter). Their  
109 center-mass position and body axis orientation were tracked in real time at 35 frames/s (**Figure 1A-**  
110 **B**). This information was used to deliver a body-centered visual stimulus using a video-projector  
111 directed onto a screen supporting the Petri dish.

112 Prior to each phototactic assay, the larva was allowed an  $\approx 8$  min-long period of spontaneous  
113 exploration under uniform and constant illumination at maximum intensity  $I_{max} = 450\mu W.cm^{-2}$ .  
114 Such pre-conditioning phases were used to promote light-seeking behavior (**Burgess and Granato,**  
115 **2007**), while enabling the quantification of the basal exploratory kinematics for each fish.

116 Larval zebrafish navigation is comprised of discrete swim bouts lasting  $\approx 100ms$  and interspersed  
117 with 1 to 2s-long inter-bout intervals ( $\tau_n$ ) during which the fish remains still (**Dunn et al., 2016**). Each  
118 bout results in a translational motion of the animal and/or a change in its body axis orientation, and  
119 can thus be automatically detected from kinematic parameters. As we are mostly interested in the  
120 orientational dynamics, we extracted a discrete sequence of orientations  $\alpha_n$  measured just before  
121 each swimming event  $n$  (**Figure 1B-C**) from which we computed the bout-induced reorientation  
122 angles  $\delta\alpha_n = \alpha_{n+1} - \alpha_n$ .

123 Although the complete swim bouts repertoire of zebrafish larvae is rich and complex (**Marques**  
124 **et al., 2018; Johnson et al., 2019**), the statistical distribution of the reorientation angles  $P(\delta\alpha_n)$  in  
125 such unbiased conditions can be correctly captured by the weighted sum of two zero-mean normal  
126 distributions,  $P(\delta\alpha_n) = p_{turn}\mathcal{N}(0, \sigma_{turn}^2) + p_{fwd}\mathcal{N}(0, \sigma_{fwd}^2)$ , reflecting the predominance of only two  
127 distinct bouts types: turning bouts (standard deviation  $\sigma_{turn} = 0.6$ ) and forward scoots ( $\sigma_{fwd} = 0.1$ )  
128 (**Figure 1D**). This bimodal distribution is consistent with the locomotor repertoire of larvae described  
129 by Marques et al. during spontaneous swimming and phototactic tasks (**Marques et al., 2018**). In the  
130 absence of a visual bias, the turning bouts and forward scoots were found to be nearly equiprobable,  
131  $p_{turn} = 1 - p_{fwd} = 0.41$ .

132 Successive bouts were found to exhibit a slightly positive correlation in amplitude (**Figure 1F**).  
133 This process can be captured by a 2-state Markov chain model that controls the alternation between  
134 forward and turning bouts, while the amplitude within each population is randomly sampled  
135 from the corresponding distribution (**Figure 1E**). Within this scheme, we analytically derived the  
136 dependence in the amplitude of successive bouts and thus estimated the forward-to-turn and  
137 turn-to-forward transition rates, noted  $k_{f\rightarrow t}$  and  $k_{t\rightarrow f}$ . We found that  $k_{f\rightarrow t}/p_{turn} = k_{t\rightarrow f}/p_{fwd} \approx 0.8$ .  
138 This indicates that the probability to trigger a turn (resp. forward) bout is decreased by only 20% if  
139 the previous bout is a forward (resp. turn) bout. For the sake of simplicity, we ignore in the following  
140 this modest bias in bout selection and assume that the chaining of forward and turning bout is

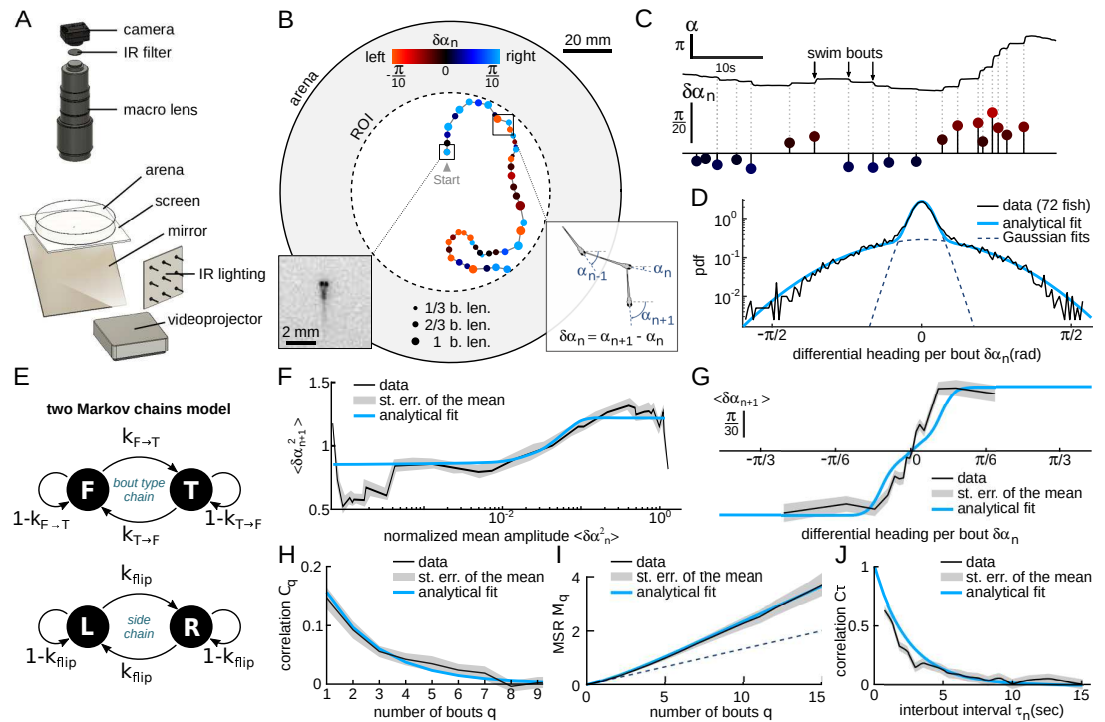


**Figure 1.** Kinematics of spontaneous navigation. (A) Experimental setup: real-time monitoring of the larva position and orientation using IR illumination, enables closed-loop visual stimulation using a video projector. (B) Typical trajectory of a 6 days old larva in the region of interest (ROI) of the arena under constant, uniform illumination. Each point indicates the fish position at the onset of a swim bout. Dots' size and color encode the bout distance and bout reorientation angle, respectively. Insets: blow-up of an example frame (*left*) and definition of the reorientation angle  $\delta\alpha_n$  at bout number  $n$  (*right*). b.len : body length. (C) Time-sequence of the fish body orientation  $\alpha$  (top). Swim bouts elicit rapid re-orientations. The angular dynamics can thus be represented as a series of discrete reorientation events of various amplitudes  $\delta\alpha_n$ , (color code as in (B)). (D) Experimental (dark) and analytical (blue) distributions (*pdf*: probability density function) of reorientations  $\delta\alpha_n$ . The two normal distributions used in the fit with **Equation A1**, weighted by  $p_{turn}$  and  $1 - p_{turn}$ , are also displayed in dashed blue lines. (E) Two independent Markov chains model for spontaneous navigation: the *bout type* chain controls the forward scoot (*F*) versus turning (*T*) state, with transitions rates  $k_{T \rightarrow F}$  and  $k_{F \rightarrow T}$ . The *side* chain controls the transitions between left (*L*) and right (*R*) headings when the animal is in the turning state, with transition rate  $k_{flip}$ . (F) Mean squared reorientation amplitude of bout  $n + 1$  as a function of the squared amplitude of bout  $n$  (grey), and its associated analytical fit (blue, **Appendix 1 Equation A5**). (G) Average reorientation of bout  $n + 1$  as a function of the reorientation at bout  $n$  (grey), and its associated analytical fit (blue, **Equation A11**). (H) Correlation in reorientation angles  $C_q$  as a function of the number of bouts  $q$  and associated fit (blue, **Equation A14**). (I) Mean square reorientation (MSR)  $M_q$  as a function of the cumulative number of bouts, and associated fit (blue, **Equation A16**). The dotted line is the linear extrapolation of the first two data points and corresponds to the diffusive process expected for a memory-less random walk (no correlation in bout orientation). (J) Orientation correlation of turning bouts (thresholded at  $0.22rad$ ) as a function of the time elapsed between those bouts. The blue line is the exponential fit.

141 memory-less by setting  $k_{f \rightarrow t} = p_{turn}$  and  $k_{t \rightarrow f} = p_{fwd}$ .

142 In line with previous observations (Chen and Engert, 2014; Dunn et al., 2016), we also noticed  
143 that successive turning bouts tended to be oriented in the same (left or right) direction (Figure 1G).  
144 This orientational motor persistence was accounted for by a second Markov chain that sets the  
145 orientation of turning bouts, and is controlled by the rate of flipping direction noted  $k_{flip}$  (Figure 1E  
146 bottom). Notice that, in contrast with the model proposed by (Dunn et al., 2016), although the  
147 orientational state is updated at each bout, it only governs the direction of turning bouts. When a  
148 forward bout is triggered, its orientation is thus unbiased.

149 This model provides an analytical prediction for the mean reorientation angle  $\langle \delta\alpha_n \rangle_{|\delta\alpha_{n-1}}$  at bout  
150  $n$  following a reorientation angle  $\delta\alpha_{n-1}$  at bout  $n - 1$  (see Annex 1). This expression was used to  
151 fit the experimental data (Figure 1G) and allowed us to estimate the flipping rate  $p_{flip} = 0.19$  (99%  
152 confidence bounds  $\pm 0.017$ ). We further computed the autocorrelation function of the reorientation  
153 angles and the Mean Square Reorientation (MSR) accumulated after  $n$  bouts (Figure 1H-I). Both were  
154 consistent with their experimental counterparts. In particular, this model quantitatively captures  
155 the ballistic-to-diffusive transition that stems from the directional persistence of successive bouts  
156 (Figure 1I). As a consequence, the effective rotational diffusivity at long time  $D_{eff} = 0.3rad^2$  is about  
157 twice as large than the value expected for a memory-less random walk with  $p_{flip} = 0.5$  (Figure 1I  
158 dashed line).

159 In this discrete Markov-chain model, time is not measured in seconds but corresponds to the  
160 number of swim bouts. It thus implicitly ignores any dependence of the transition rates with the  
161 interbout interval. We examined this hypothesis by evaluating the correlation in bouts orientations  
162 as a function of the time elapsed between them. To do so, we first selected the putative turning  
163 bouts by selecting the large amplitude events ( $|\delta\alpha| < 0.22rad$ ). We then binarized their values, based  
164 on their leftward or rightward orientation, yielding a discrete binary signal  $s(t_n) = \pm 1$ . We finally  
165 computed the mean product  $\langle s(t_n)s(t_p) \rangle$  for various time intervals  $\Delta t = t_p - t_n$ . The resulting graph,  
166 shown in Figure 1J, demonstrates that the correlation in orientation of successive bouts decays  
167 quasi-exponentially with the inter-bout period. This mechanism can be captured by assuming that  
168 the orientation selection at each bout is governed by a hidden two-state continuous-time process.  
169 The simplest one compatible with our observations is the telegraph process, whose transition  
170 probability over a small interval  $dt$  reads  $k_{flip}dt$ , and whose autocorrelation decays as  $\exp(-2k_{flip}t)$ .  
171 Setting  $k_{flip} = p_{flip}/median(\tau_n) = 0.2s^{-1}$ , this model thus correctly captures the  $\tau_n$ -dependence of the  
172 orientational correlation of bouts.

173 In the two following sections, we use the discrete version of the Markov-model to represent  
174 the fish navigation, and investigate how the model's parameters are modulated in the presence of  
175 a virtual distant light source. We then go back to the underlying continuous-time process when  
176 introducing a neuronal rate model for the orientation selection process.

### 177 Contrast-driven phototaxis can be described as a biased random walk

178 We first examined the situation in which the perceived stereo-visual contrast is the only cue  
179 accessible to the animal to infer the direction of the light source (tropotaxis regime). The visual  
180 stimulus consisted of two uniformly lit half-disks, each covering one visual hemifield. The intensity  
181 delivered to the left and right eyes, noted  $I_L$  and  $I_R$  respectively, were locked onto the fish's  
182 orientation relative to the virtual light source  $\theta$  (Figure 2A-C): the total intensity ( $I_L + I_R$ ) was  
183 maintained constant while the contrast  $c = I_L - I_R$  was varied linearly with  $\theta$ , with a mirror symmetry  
184 at  $\pi/2$  (Figure 2B). This dependence was chosen to mimic the presence of a distant source located  
185 at  $\theta = 0$  (Figure 2B), for which the contrast is null.

186 The orientation of the virtual source in the laboratory frame of reference was randomly selected  
187 at initiation of each assay. After only a few bouts, the animal orientation was found to be statistically  
188 biased towards  $\theta = 0$ , as shown in Figure 2C-D. This bias was quantified by computing the population  
189 resultant vector  $R$  defined as the vectorial mean of all orientations (Figure 2E).

190 Trajectories that are strongly biased towards the source tend to exit the ROI earlier than unbiased

191 trajectories, which are more tortuous and thus more spatially confined. This generates a progressive  
192 selection bias as the number of bouts considered is increased, as revealed by the slow decay of the  
193 resultant vector length (**Figure 2–Figure Supplement 1**). In order to mitigate this selection bias, all  
194 analyses of stationary distributions were restricted to bout indices lower than the median number  
195 of bouts per trial ( $N \leq 17$ ), and excluding the first bout. Under this condition, we found that  $\sim 77\%$  of  
196 zebrafish larvae display a significant phototactic behavior (**Figure 2D**, test of significance based on a  
197 combination of two circular statistic tests, see *Methods*), a fraction consistent with values reported  
198 by **Burgess et al. (2010)** in actual phototactic assays .

199 From these recordings, we could characterize how the contrast experienced during the inter-bout  
200 interval impacts the statistics of the forthcoming bout. **Figure 2G** displays the mean reorientation  
201  $\delta\theta$  as a function of the instantaneous contrast  $c$ . This graph reveals a quasi-linear dependence  
202 of the mean reorientation with  $c$ , directed towards the brighter side. Notice that the associated  
203 slope shows a significant decrease in the few first bouts, before reaching a quasi-constant value  
204 (**Figure 2–Figure Supplement 2**). This effect likely reflects a short term habituation mechanism, as  
205 the overall intensity drops by a factor of 2 at the initiation of the assay.

206 For a more thorough analysis of the bout selection mechanisms leading to the orientational  
207 bias, we examined, for all values of the contrast, the mean and variance of the two distributions  
208 associated with turning bouts and forward scoots, as well as the fraction of turning bouts  $p_{turn}$   
209 (**Figure 2H–K**). We found that the orientational drift solely results from a probabilistic bias in the  
210 selection of the turning bouts (left vs right) orientation: the mean orientation of the turning bouts  
211 varies linearly with the imposed contrast (**Figure 2I**). Reversely, the ratio of turning bouts and the  
212 variance of the two distributions are insensitive to the contrast (**Figure 2J–K**). These results indicate  
213 that the stereo-visual contrast has no impact neither on bout type selection nor on bout amplitude.

214 As discussed in the preceding section, successive bouts tend to be oriented in the same direction.  
215 During phototaxis, the selection of the turning orientation is thus expected to reflect a competition  
216 between two distinct mechanisms: motor persistence, which favors the previous bout orientation,  
217 and stereo-visual bias, which favors the brighter side. To investigate how these two processes  
218 interfere, we sorted the bouts into two categories. In the first one, called "reinforcement", the  
219 bright side is in the direction of the previous bout, such that both the motor and sensory cues act  
220 in concert. In the second one, called "conflicting", the contrast tends to evoke a turning bout in a  
221 direction opposite to the previous one. For each category, we plotted the mean reorientation angle  
222 at bout  $n$  as a function of the reorientation angle at bout  $n - 1$  (**Figure 2L**). We further estimated, for  
223 each condition and each value of the contrast, the probability of flipping orientation  $p_{flip}$  (**Figure 2M**  
224 and *Methods*). These two graphs show that the stereo-visual contrast continuously modulates the  
225 innate motor program by increasing or decreasing the probability of flipping bout orientation from  
226 left to right and *vice versa*. Noticeably, in the conflicting situation at maximum contrast, the visual  
227 cue and motor persistence almost cancel each other out such that the mean orientation is close to  
228 0 ( $p_{flip} \sim 0.4$ ).

### 229 **Phototaxis under uniform stimulation is driven by a modulation of the orienta-** 230 **tional diffusivity**

231 We now turn to the second paradigm, in which the stereo-visual contrast is null (both eyes receive  
232 the same illumination at any time), but the total perceived illumination is orientation-dependent  
233 (klinotaxis regime). We thus imposed a uniform illumination to the fish whose intensity  $I$  was locked  
234 onto the fish orientation  $\theta$  relative to a virtual light source. We tested three different illumination  
235 profiles  $I(\theta)$  as shown in **Figure 3A**: a sinusoidal and two exponential profiles with different maxima.  
236 Despite the absence of any direct orientational cue, a large majority of the larvae (78%) displayed  
237 positive phototactic behavior: their orientational distribution showed a significant bias towards the  
238 virtual light source, *i.e.* the direction of maximum intensity (**Figure 3C–E**).

239 Although the efficiency of the phototactic behavior is comparable to the tropotaxis case previ-  
240 ously examined, here we did not observe any systematic bias of the reorientation bouts towards

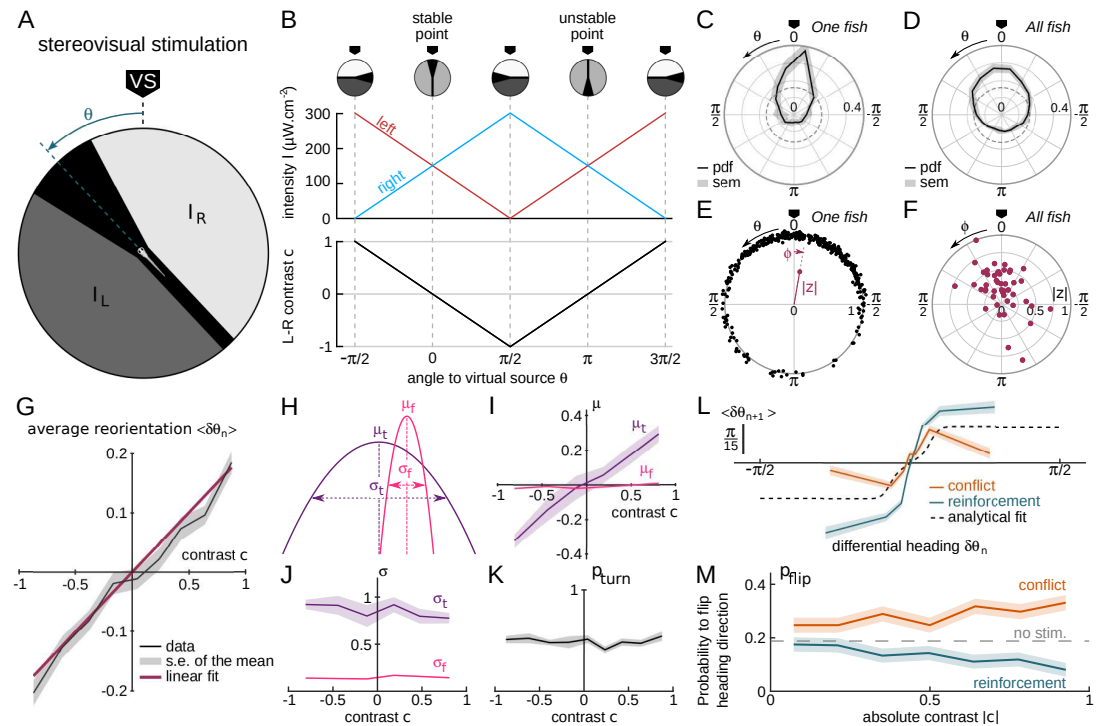


**Figure 2.** Contrast-driven phototaxis as a biased random walk.  $N = 47$  fish, 18,322 bouts. All statistical analysis are performed on the first 17 bouts, the first one excluded, for each assay. VS : virtual source. (A) Stimulus pattern delivered to the larva. The orientation relative to the virtual source is noted  $\theta$ . (B) Left and right intensities (top panel) and contrast  $c = \frac{I_L - I_R}{I_L + I_R}$  (bottom panel) as a function of  $\theta$ . The virtual light source is defined by a null contrast ( $c = 0$ ) and corresponds to a stable point ( $\frac{dc}{d\theta} < 0$ ). (C) Probability density function (pdf) of orientations relative to the virtual light source for one fish during 20 trials, bouts 2 to 17 ( $n=320$  bouts). (D) Probability density function (pdf) of orientations for all tested fish ( $N = 47$ ). Significantly biased toward the virtual source (V-test for non-uniformity with specified mean 0 ( $p_{val} < 10^{-11}$ )). (E) Definition of the mean resultant vector length  $R$  for one fish. The points represent the angular positions  $\theta_n$  of the fish relative to the source. The length of the resultant vector is defined, in the complex plane, as  $R = \left| \frac{1}{N} \sum \exp i\theta_n \right|$ . (F) Resultant vectors  $R$  for individual fish. (G) Mean reorientation  $\langle \delta\theta_n \rangle$  per bout as a function of contrast  $c$  for all fish. Error bars represent the standard error of the mean. Red line is the linear fit with slope 0.2 rad. (H) Illustration of the shift in turning distribution ( $\mu_t < 0$ ) induced by a negative contrast. (I) Means, (J) standard deviations and (K) relative weight of the turning distribution as a function of the contrast. For each value of the contrast, these quantities were extracted by double-Gaussian fitting of the bout angles. The error bars represent the 99% confidence interval from the fit. (L) Average reorientation at bout  $n + 1$  as a function of the reorientation at bout  $n$  in reinforcing (contrast and previous bout orientation are consistent) or conflicting (contrast and previous bout orientation are in conflict) situations. The dashed line is the analytical prediction in the absence of stimulation. (M) Probability of switching direction  $p_{flip}$  as a function of the contrast, in situations of conflict or reinforcement.

**Figure 2-Figure supplement 1.** Evolution of  $R$  as a function of bout number

**Figure 2-Figure supplement 2.** Evolution of bias slope with bout number

241 the brightest direction (**Figure 3F**). This indicates that the larvae do not use the change in intensity  
242 at a given bout to infer the orientation of the source in order to bias the orientation of the forth-  
243 coming turn. Instead, the phototactic process originates from a visually-driven modulation of the  
244 orientational diffusivity, as measured by the variance of the bout angle distributions (**Figure 3G**).  
245 The use of different profiles allowed us to identify which particular feature of the visual stimulus  
246 drives this modulation. Although the bout amplitude variance was dependent on the intensity  $I$  and  
247 intensity change  $\delta I$  experienced before the bout, these relationships were found to be inconsistent  
248 across the different imposed intensity profiles. In contrast, when plotted as a function of  $\delta I/I$ , all  
249 curves collapse (**Figure 3–Figure Supplement 1**). This observation is in line with the Weber-Fechner  
250 law (**Fechner, 1860**), which states that the perceived change scales with the relative change in the  
251 physical stimulus. One noticeable feature of this process is that the modulation of the turning  
252 amplitude is limited to illumination *decrement* (*i.e.* negative values of  $\delta I/I$ ). In the terminology  
253 of bacterial chemotaxis (**Oliveira et al., 2016**), the zebrafish larva can thus be considered as a  
254 "pessimistic" phototactic animal: the orientational diffusivity increases in response to a decrease  
255 in illumination (corresponding to a negative subjective value), whereas its exploratory kinematics  
256 remain unchanged upon an increase of illumination (positive subjective value).

257 Two kinematic parameters can possibly impact the orientational diffusivity: the fraction of  
258 turning bouts  $p_{turn}$  and their characteristic amplitude  $\sigma_{turn}$ . We thus extracted these two quantities  
259 and plotted them as a function of  $\delta I/I$  (**Figure 3G-H**). They appear to equally contribute to the  
260 observed modulation.

261 To test whether this uniform phototactic process has a retinal origin, or whether it might be  
262 mediated by non-visual deep-brain photoreceptors (**Fernandes et al., 2013**), we ran similar assays  
263 on bi-nucleated fish. In this condition, no orientational bias was observed, which indicates that  
264 the retinal pathway is involved in the orientational klinotaxis (**Figure 3–Figure Supplement 2**, all  
265  $p$ -values  $> 0.14$ , pairwise  $T$ -tests).

## 266 **A biased random walk model for phototaxis provides a quantitative prediction of** 267 **light-driven orientational bias**

268 In the preceding sections, we quantified how visual stimuli stochastically modulate specific kinematic  
269 parameters of the subsequent bout. We used these relationships to build a biased random walk  
270 model of phototaxis. We then tested how such a model could reproduce the statistical orientational  
271 biases towards the directions of minimal contrast and maximal illumination. The phototactic  
272 model thus incorporates a visually-driven bias to the discrete two-Markov chains introduced to  
273 represent the spontaneous navigation (**Figure 4A**). In line with the observation of **Figure 2M**, the  
274 rate of flipping orientational state (left-to-right or right-to-left) was a linear function of the imposed  
275 contrast:  $k_{R \rightarrow L} = k_{flip} + ac$  and  $k_{L \rightarrow R} = k_{flip} - ac$ . The value of  $a$  was set so as to capture the contrast-  
276 dependent orientational drift (**Figure 2G**) and was made dependent on bout number in order to  
277 account for the observed habituation process (**Figure 2–Figure Supplement 2**).

278 The selection of bout type was in turn linearly modulated by the relative change in intensity  
279 after negative rectification ( $[\delta I/I]^- = \min(\delta I/I, 0)$ ). Hence, the turn-to-forward and forward-to-turn  
280 transition rates read  $k_{t \rightarrow f} = k_{turn} + \beta [\delta I/I]^-$  and  $k_{f \rightarrow t} = k_{turn} - \beta [\delta I/I]^-$ , respectively. We also  
281 imposed a linear modulation of the turn amplitude variance  $\sigma_{turn} = \sigma_{turn}^{spont} - \gamma [\delta I/I]^-$ . The values of  $\beta$   
282 and  $\gamma$  were adjusted to reproduce the observed dependence of the turn-vs-forward ratio and bout  
283 amplitude with  $\delta I/I$  (**Figure 3H-I**).

284 This stochastic model was tested under two conditions, tropo- and klino-phototaxis, similar to  
285 those probed in the experiments (**Figure 4B**). In order to account for the sampling bias associated  
286 with the finite size of the experimental ROI, the particles in the simulations also progressed in a 2D  
287 arena. At each time step, a forward displacement was drawn from a gamma distribution adjusted  
288 on the experimental data (**Figure 5–Figure Supplement 1**). Statistical analysis was restricted to  
289 bouts executed within a circular ROI as in the experimental assay.

290 The comparison of the data and numerical simulation is shown in **Figure 4C** for the tropotaxis

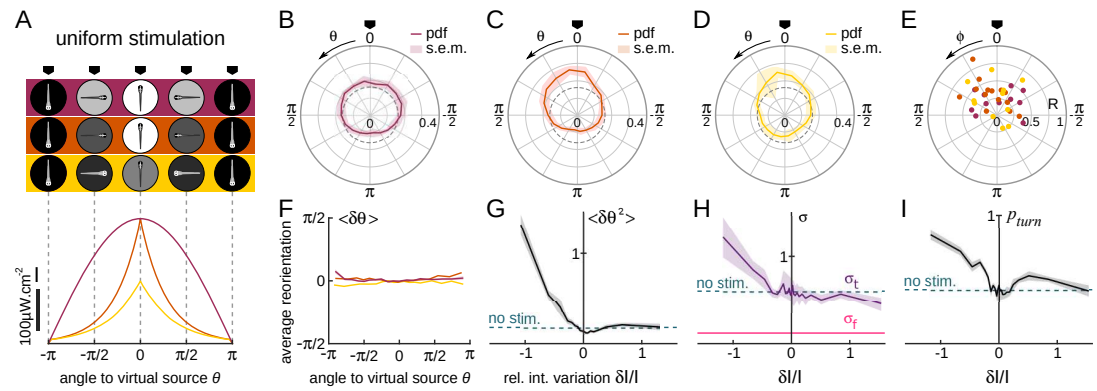


**Figure 3.** Orientational phototaxis driven by modulation of the global illumination.  $N = 37$  fish,  $n = 26,443$  bouts. (A) Top panel : Angle-dependent intensity profiles delivered to the larva. The virtual light source is located at  $\theta = 0$ , defined as the point of maximum intensity. The profiles are sinusoidal (uniform 1, purple) or exponentially-shaped (uniform 2 and 3 respectively orange and yellow). All statistics were computed using bouts number 2 to the median number of bouts per sequence (resp. 27, 17 and 15 for the 3 profiles). (B-D) PDF of the fish orientations for the 3 profiles. All 3 distributions are significantly biased towards the virtual source (V-test for non-uniformity of circular data with specified mean 0,  $p_{vals}$  respectively  $9.10^{-3}$ ,  $2.10^{-7}$  and  $3.10^{-5}$ ). (E) Resultant vector  $\mathbf{R}$  for all individual fish. (F) Mean reorientation per bout  $\langle \delta\theta \rangle$  of all fish as a function of  $\theta$  for the 3 profiles. No significant bias towards the source ( $\theta = 0$ ) is observed. (G) Variance of the reorientation angles  $\langle \delta\theta^2 \rangle$  as a function of the relative change in intensity experienced at the previous bout  $\delta I/I$ . Error bars are standard error of the mean. (H) Standard deviation  $\sigma_{turn}$  of turning bouts as a function of  $\delta I/I$ . The standard deviation of forward scouts was set at  $\sigma_{fwd}$ , and  $\sigma_{turn}$  was then estimated using a double-Gaussian fitting of the bout angles. Error bars are the 99% confidence interval from fit. (I) Probability of triggering a turning bout as a function of  $\delta I/I$ . Error bars are the 99% confidence interval from the fit.

**Figure 3-Figure supplement 1.** Variance of  $\delta\theta$  as a function of 3 different illumination parameters

**Figure 3-Figure supplement 2.** Control for retinal origin of klinotaxis

291 protocol and in **Figure 4D-F** for the klinotaxis protocols. This minimal stochastic model quantitatively  
 292 captures the mean orientational bias, as measured by the resultant vector  $\mathbf{R}$ . It also reproduces the  
 293 evolution of this parameter as a function of the cumulative number of bouts (**Figure 4G-J**).

294 **A neuronal model of the ARTR captures spontaneous and contrast driven navigation**  
 295 **tion**

296 The behavioral description proposed above indicates that larvae navigation can be correctly ac-  
 297 counted for by two independent stochastic processes: one that organizes the sequence of succes-  
 298 sive bouts amplitude and in particular the selection of forward vs turning events, while a second  
 299 one selects the left vs right orientation of the turning bouts. These two processes are independently  
 300 modulated by two distinct features of the visual stimulus, namely the global intensity changes and  
 301 the stereo-visual contrast, leading to the two phototactic strategies.

302 This in turn suggests that, at the neuronal level, two independent circuits may control these  
 303 characteristics of the executed swim bouts. As mentioned in the introduction, the ARTR is a  
 304 natural candidate for the neuronal selection of bouts orientation. This small bilaterally-distributed  
 305 circuit located in the anterior hindbrain displays antiphase activity oscillation with  $\sim 20s$  period  
 306 (**Ahrens et al., 2013**). The currently active region (left or right) constitutes a strong predictor of the  
 307 orientation of turning bouts (**Dunn et al., 2016**). This circuit further integrates visual inputs as each  
 308 ARTR subpopulation responds to the uniform stimulation of the ipsilateral eye (**Wolf et al., 2017**).

309 Here we adapted a minimal neuronal model of the ARTR, introduced in **Wolf et al. (2017)**  
 310 to interpret the calcium recordings, and tested whether it could explain the observed statistics  
 311 of exploration in both spontaneous and phototactic conditions. The architecture of the model  
 312 is depicted in **Figure 5A**. The network consists of two modules that are selective for leftward  
 313 and rightward turning bouts, respectively. A perfect candidate mechanism for the generation of

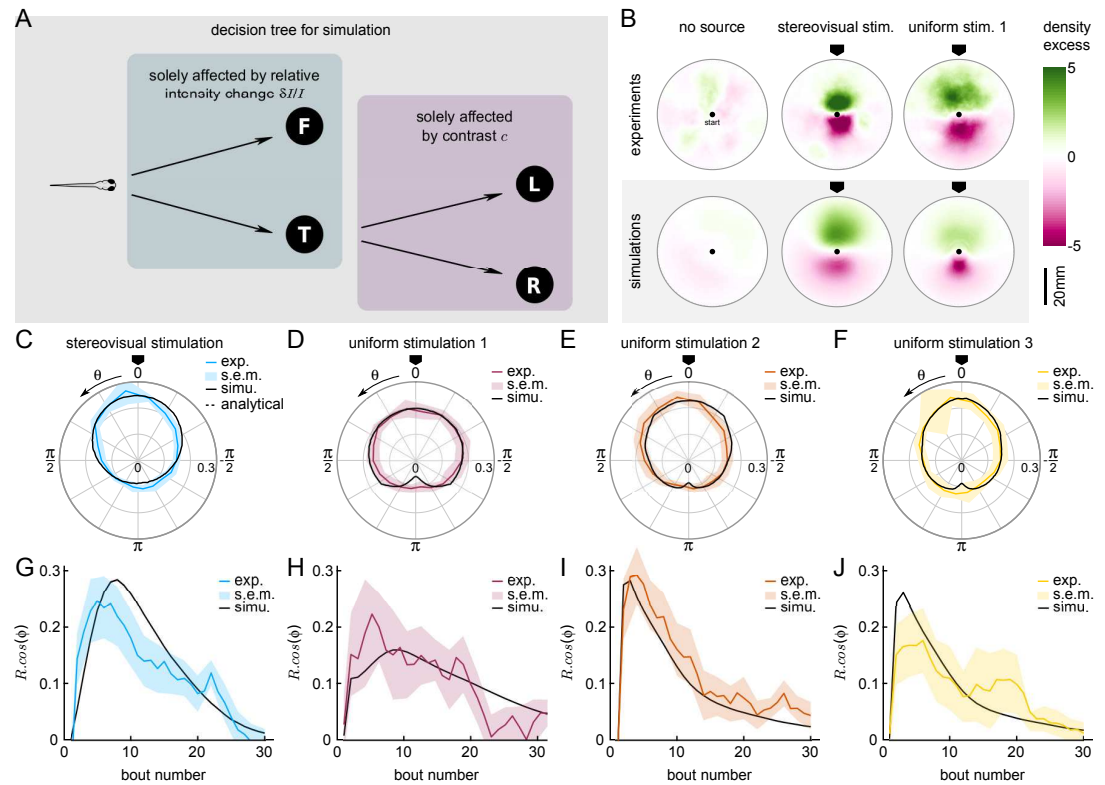


**Figure 4.** A Markov-chain model of phototaxis captures the observed orientational distribution. (A) Decision tree for simulation: selection of forward scoots vs turning bouts are governed by the relative intensity change at the previous bout. If a turning bout is triggered, the selection of left-right orientation is biased by the stereovisual contrast. (B) 2D density profiles computed from all experimental and simulated trajectories for the three different paradigms (no stimulation, lateralized illumination and uniform illumination). The color encodes the excess or deficit of density with respect to the radially-averaged density without any stimulation. (C-F) Experimental (color) and simulation (solid line) probability density distributions of orientations for the 4 phototactic configurations (stereo-visual stimulation, uniform stimulation with angular profiles 1 to 3). (G-J) Evolution of the resultant vector's length as a function of the bout number for the experiment (color) and simulation (solid line). Error bar : standard error of the mean.

314 persistent activity is strong recurrent excitation in each module through recurrent coupling ( $w_E$ ),  
315 this tends to maintain each module's activity for a finite period of time. Reciprocal inhibition ( $w_I$ )  
316 between the left and right modules guarantees strong antiphasic dynamics between each side.  
317 Finally, each ARTR module receives an input current from the visual system proportional to the  
318 illumination of the ipsilateral eye. Such architecture gives rise to a stimulus-selective attractor well  
319 described in *Freeman (1995); Wang (2001)*.

320 The equations governing the network are provided in Appendix 2 *Equation A17*. The various  
321 model parameters were adjusted in order to match the behavioral data. First, the self-excitatory  
322 and cross-inhibitory couplings were chosen such that the circuit displayed spontaneous oscillatory  
323 dynamics in the absence of sensory input. *Figure 5B* shows example traces of the two units' activity  
324 in this particular regime. From these two traces, we extracted a binary "orientational state" signal  
325 by assigning to each time point a left or right value (indicated in red and blue, respectively), based  
326 on the identity of the module with the largest activity.

327 In the present approach, tail bouts are assumed to be triggered independently of the ARTR  
328 activity. The latter thus acts as mere orientational hub by selecting the orientation of the turning  
329 events: incoming bouts are oriented in the direction associated with the currently active module.  
330 In the absence of information regarding the circuit that organizes the swim bouts emission, their  
331 timing and absolute amplitude were drawn from the behavioral recordings of freely swimming  
332 larvae (*Figure 5*- figure supplement 1). Combined with the ARTR dynamics, this yielded a discrete  
333 sequence of simulated bouts (leftward, rightward and forward, *Figure 5B*, inset). With adequate  
334 choice of parameters, this model captures the orientational persistence mechanism, as quantified  
335 by the slow decay of the turning bout autocorrelation with the interbout interval (*Figure 5C*).

336 In the presence of a lateralized visual stimulus, the oscillatory dynamics become biased towards  
337 the brightest direction (*Figure 5D-E*). Hence, illuminating the right eye favors longer periods of  
338 activation of the rightward-selective ARTR unit. The mean reorientation displays a quasi-linear  
339 dependence with the imposed contrast (*Figure 5D*) in line with the behavioral observations (*Fig-  
340 ure 2G*). At intermediate contrast values, the orientation of bouts remains stochastic; the effect of  
341 the contrast is to lengthen streaks of turning bouts towards the light (*Figure 5E*). We also tested  
342 whether this model could capture the competition mechanism between stereovisual bias and motor  
343 persistence, in both conflicting and reinforcement conditions. We thus computed the dependence  
344 of the flipping probability  $p_{flip}$  as a function of the contrast in both conditions (*Figure 5F*). The  
345 resulting graph is in quantitative agreement with its experimental counterparts (*Figure 2M*).

346 We finally used this model to emulate a simulated phototactic task. In order to do so, a virtual  
347 fish was submitted to a contrast whose amplitude varied linearly with the animal orientation, as  
348 in the lateralized assay. When a turning bout was triggered, its orientation was set by the ARTR  
349 instantaneous activity while its amplitude was drawn from the experimental distributions. After a  
350 few bouts, a stationary distribution of orientation was reached that was biased towards the virtual  
351 light source (*Figure 5G*). Its profile was in quantitative agreement with its experimental counterpart  
352 (mean resultant vector length  $R = 0.23$  in simulation for  $R = 0.24$  in experimental data for bouts 2  
353 to 17).

## 354 Discussion

355 Sensorimotor transformation can be viewed as an operation of massive dimensionality reduction, in  
356 which a continuous stream of sensory and motor-related signals is converted into a discrete series of  
357 stereotyped motor actions. The challenge in understanding this process is (i) to correctly categorize  
358 the behavioral events, *i.e.* to reveal the correct parametrization of the motor repertoire, and (ii) to  
359 unveil the statistical rules for action selection. Testing the validity of such description can be done  
360 by building a minimal model based on these rules. If the model is correct, the motor variability  
361 unaccounted for by the model should be entirely random, *i.e.* independent of the sensorimotor  
362 history.

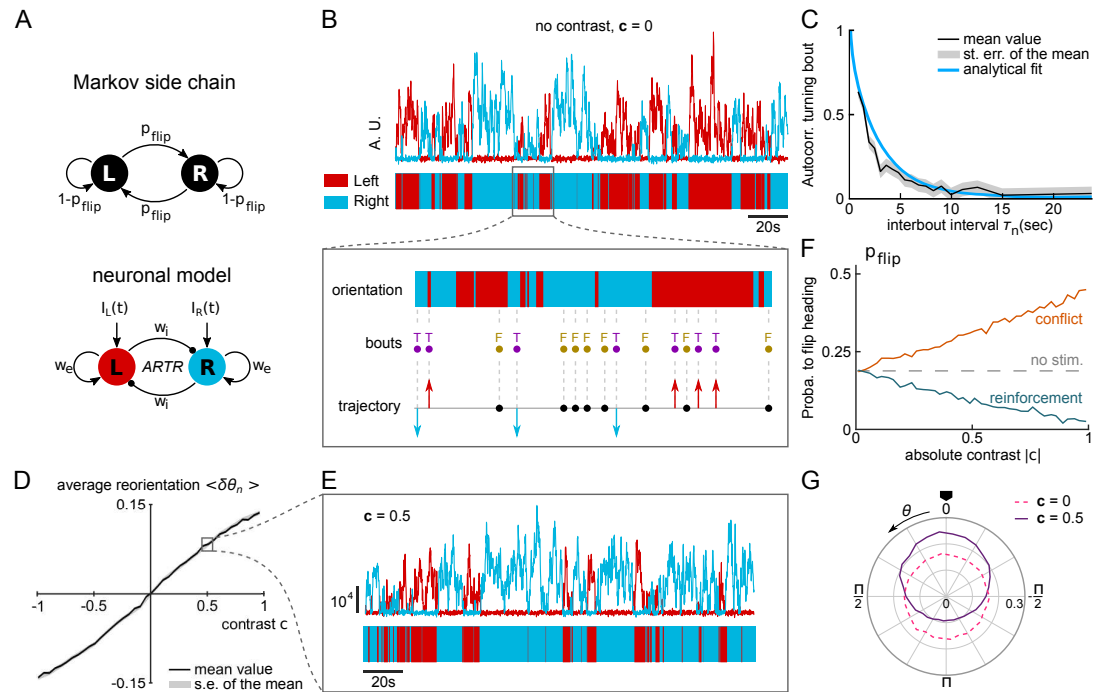


**Figure 5.** A neuronal model of turning bout selection captures spontaneous and contrast-driven navigation. (A) Scheme of the Markov chain model of the orientation selection, and corresponding neuronal model of the ARTR. The latter consists of two units whose relative activation controls the orientation of bouts. Persistent and self-alternating dynamics result from the recurrent excitation ( $w_E$ ) and reciprocal inhibition ( $w_I$ ) between each unit. They further receive input currents proportional to the illumination of the ipsilateral eye. (B) Top: example traces of the simulated activity of the left (red) and right (blue) modules in the absence visual stimulation (AU : arbitrary units). These continuous dynamics control the alternation between right and left orientational states. Close-up: forward and turning bouts are triggered independently with a statistics drawn from the behavioral recordings. The orientational state governs the orientation of the turning bouts. (C) Orientation correlation of turning bouts (thresholded at .22 rad) as a function of the inter-bout interval  $\tau_n$ . Result from the neuronal model is in blue, experimental data are in black. (D) Mean reorientation  $\langle \delta\theta \rangle$  as a function of the contrast  $c$ . (E) Example traces of the simulated activity for a constant contrast  $c = 0.5$ . (F) Probability of flipping orientation as a function of the imposed contrast  $c$  in situations of conflict or reinforcement (neuronal model). (G) Probability distribution function of  $\theta$  for 10 simulated phototactic trajectories with a linear dependence of average reorientation on contrast. Each trajectory lasted 50,000 seconds. The dotted line is the orientational distribution in the absence of visual stimulation.

**Figure 5-Figure supplement 1.** Inter-bout distance distribution

**Figure 5-Figure supplement 2.** Simulated trajectories with different inter-bout intervals  $\tau_n$

363 Here we implemented a minimal model approach in order to unveil the basic rules underlying  
364 phototaxis. We showed that zebrafish light-driven orientational navigation can be quantitatively  
365 described by a stochastic model consisting of two independent Markov chains: one that selects  
366 forward scoots vs turning bouts and a second one that sets the orientation of the latter. We  
367 established that the stereo-visual contrast and global intensity modulation act separately on each  
368 of these selection processes. The contrast induces a directed bias of turning bouts towards  
369 the illuminated side, but does not impact the prevalence of turning bouts vs forward scoots.  
370 Reversely, a global decrement in illumination increases the ratio of turning bouts but does not  
371 favor any particular direction. For the contrast-driven configuration (tropotaxis), the minimal model  
372 corresponds to an Ornstein-Uhlenbeck process (*Uhlenbeck and Ornstein, 1930*), which describes  
373 the dynamics of a diffusive brownian particle in a quadratic trap. In the klinotaxis configuration (in  
374 the absence of stereo-visual contrast), the orientational bias solely results from a light-dependent  
375 modulation of the diffusivity, a mechanism reminiscent of bacterial chemotaxis.

376 This stochastic minimal model is built on a simple decision tree (*Figure 4A*) with a set of binary  
377 choices. However, to fully capture the orientational dynamics, we had to incorporate the continuous  
378 increase in turning bout amplitude with the light decrement in an ad-hoc way. It is currently unclear  
379 whether all turn bouts in our experiments can be assigned to a single class of swim maneuvers that  
380 are modulated in amplitude, or whether these encompass distinct motor programs executed with  
381 varying frequencies. In the latter case, it might be possible to represent this amplitude modulation  
382 through an extension of the decision tree that would select between distinct turn bout categories.

383 Compared to previous studies on phototaxis, e.g. *Burgess et al. (2010)*, our approach allowed  
384 us to clearly disentangle the contributions of spatial (stereovisual contrast) and time-dependent  
385 (motion-induced change in global illumination) visual cues. Hence, the contrast-driven assays were  
386 performed under constant overall illumination intensity (the sum of left and right intensities). This  
387 allowed us to establish that, rather surprisingly, the probability of triggering a turn (vs a forward  
388 swim) is insensitive to the imposed contrast. This possibility constitutes an important asset with  
389 respect to standard experimental configurations, such as the one examined by *Burgess et al. (2010)*,  
390 in which the animal is submitted to an actual distant light source. Although these configurations  
391 provide a more realistic context, the visual stimulus effectively perceived by each eye can not  
392 be quantitatively assessed, which precludes the design of predictive models. Conversely, once  
393 adjusted on well-controlled virtual assays, our model could be numerically implemented in realistic  
394 environments, and the trajectories could then be directly confronted with behavioral data. This  
395 would require to first infer how the intensity impinging on each eye depends on the source distance  
396 and orientation relative to the animal body axis.

397 Another critical and distinct aspect of the present work is its focus on the steady-state dynamics.  
398 Our aim was to mimic the continuous exploration of an environment in which the brightness level  
399 displays slowly varying angular modulations. The luminosity profiles were thus chosen to ensure  
400 that individual bouts elicited relatively mild changes in illumination. By doing so, we tried to mitigate  
401 visual startle responses that are known to be elicited upon sudden darkening (*Stephen S. Easter  
402 and Nicola, 1996*). Although we could not avoid the initial large drop in illumination at the onset of  
403 each trial, the associated short-term response (*i.e.* the first bout) was excluded from the analysis.  
404 In this respect, our experiment differs from the study of *Chen and Engert (2014)* in which a similar  
405 close-loop setup was used to demonstrate the ability of larvae to confine their navigation within  
406 bright regions. This behavior was entirely controlled by the animal's response to light-on or light-off  
407 stimuli as it crossed the virtual border between a bright central disk and the dark outer area. These  
408 sharp transitions resulted in clear-cut behavioral changes that lasted for a few bouts. In comparison,  
409 our experiment addresses a different regime in which subtle light-driven biases in the spontaneous  
410 exploration cumulatively drive the animal towards brightest regions.

411 As we aimed to obtain a simple and tractable kinematic description, we ignored some other  
412 aspects of the navigation characteristics. First, we focused on the orientation of the animal and thus  
413 did not systematically investigate how the forward components of the swim bouts were impacted

414 by visual stimuli. However, in the context of angle-dependent intensity profiles, this effect should  
415 not impact the observed orientational dynamics. More importantly, we ran most of our analysis  
416 using the bout number as a time-scale, and thus ignored possible light-driven modulations of the  
417 inter-bout intervals ( $\tau_n$ ). We showed, however, that the orientational correlation is controlled by  
418 an actual time-scale. This result may have significant consequence on the fish exploration. In  
419 particular, we expect that changes in bout frequency, reflecting various level of motor activity,  
420 may significantly affect the geometry of the trajectories (and not only the speed at which they are  
421 explored). We illustrated this process by running numerical experiments at similar flipping rate  $k_{flip}$   
422 for increasing bout frequencies. The trajectories, shown in **Figure 5–Figure Supplement 2**, exhibit  
423 increasing complexity as measured by the fractal dimension. This mechanism may explain the  
424 changes in trajectories' geometry observed by *Horstick et al. (2017)* in response to sudden light  
425 dimming.

426 An important outcome of this study is to show that light-seeking navigation uses visual cues over  
427 relatively short time scales. The bouts statistics could be captured with a first order autoregressive  
428 process, indicating that the stimulus perceived over one  $\tau_n$  is sufficient to predict the forthcoming  
429 bout. However, one should be aware that such observation is only valid provided that the sensory  
430 context remains relatively stable. Hence for instance, a prolonged uniform drop in luminosity is  
431 known to enhance the overall motor activity (generally measured by displacement over a period  
432 of time) for up to several tens of minutes (*Prober et al., 2006; Emran et al., 2007, 2009; Liu et al.,*  
433 *2015*). This long-term behavioral change, so-called photokinesis, might be regulated by deep brain  
434 photoreceptors (*Fernandes et al., 2013; Horstick et al., 2017*) and thus constitutes a distinct mech-  
435 anism. One particularly exciting prospect will be to understand how such behavioral plasticity may  
436 not only modulate the spontaneous activity (*Johnson et al., 2019*) but also affects the phototactic  
437 dynamics.

438 One of the motivations of minimal behavioral models is to facilitate the functional identifica-  
439 tion and modeling of neural circuits that implement the identified sensorimotor operations in  
440 the brain. Here we used the behavioral results to propose a neuronal model of the ARTR that  
441 quantitatively reproduces non-trivial aspects of the bout selection process. This recurrent neural  
442 circuit is a simplified version of working memory models developed by *Brunel and Wang (2001);*  
443 *Wang (2001, 2002, 2008)* and adapted in *Wang (2002)* for a decision task executed in the parietal  
444 cortex (*Shadlen and Newsome, 1996, 2001*). In this class of models, the binary decision process  
445 reflects the competition between two cross-inhibitory neural populations. The circuit is endowed  
446 with two major functional capacities: (1) it can maintain mnemonic persistent activity over long  
447 periods of time, thanks to recurrent excitatory inputs; (2) it can integrate sensory signals in a graded  
448 fashion to continuously bias the statistics of the decision. This model thus naturally recapitulates  
449 the major functional features of the sensory-biased Markov side chain - motor persistence and  
450 contrast-driven continuous bias - that organizes the orientation selection.

451 It is tempting to generalize about this behavior-to-circuit approach, at least in small animals such  
452 as zebrafish or drosophila, by representing any behavior as a coordinated sequence of competing  
453 elemental actions biased by sensory feedback and organized within a hierarchical decision tree.  
454 The identification of such decision trees through quantitative behavioral analysis may provide a  
455 blueprint of the brain functional organization and significantly ease the development of circuit  
456 models of brain-scale sensorimotor computation.

## 457 **Materials and methods**

### 458 **Zebrafish maintenance and behavioral setup**

459 All behavioral free-swimming experiments were performed on wild-type zebrafish (*Danio Rerio*)  
460 larvae aged 5 to 8 days post-fertilization. Larvae were reared in Petri dishes in E3 solution on a  
461 14/10h light/dark cycle at 28°C, and were fed powdered nursery food every day from 6 dpf.

462 Experiments were conducted during daytime hours (10 am to 6 pm). Single larvae were swim-

463 ming in a 14 cm in diameter Petri dish containing E3 medium. The arena was placed on a screen  
464 illuminated from below by a projector (ASUS S1). Infrared illumination was provided by LEDs, to  
465 enable recording and tracking of the fish. We used an IR-sensitive Flea3 USB3 camera (FL3-U3-  
466 13Y13M-C, Point Grey Research, Richmond, BC, Canada), with an adjustable macro lens (Zoom 7000,  
467 Navitar, USA) equipped with an IR filter.

468 The experimental setup was enclosed in a light-tight rig, which was maintained at 28°C using "The  
469 Cube" (Life Imaging Services).

470 For the stereovisual paradigm  $N = 47$  larvae were tested, and  $N = 37$  for the temporal paradigm  
471 [(uniform 1) : 12, (uniform 2) : 11, (uniform 3) : 14]. All tested fish ( $N = 84$ ) were also used to assess  
472 spontaneous navigation statistics.

### 473 Behavioral assay

474 Closed-loop tracking and illumination were performed at a mean frequency of 35 Hz, with a  
475 custom-written software in Matlab (The MathWorks), using the PsychToolBox (PTB) version 3.0.14  
476 add-on.

477 Position and orientation (heading direction) of the fish, as well as bouts characteristics, were  
478 extracted online and the illumination pattern was updated accordingly, with a maximum latency  
479 of 34ms. Heading direction was extracted with an accuracy of +/- 0.05 rad ( $\sim 3^\circ$ ). To mitigate the  
480 effects of the walls in the fish navigation, behavioral monitoring was restricted to a circular central  
481 region of interest of 8.2cm diameter. When outside the ROI, the fish was actively brought back  
482 into the field of view of the camera through the opto-motor reflex (OMR), using a concentrically  
483 moving circular pattern. One second after the fish re-entered the ROI, a new recording sequence  
484 was started.

485 Prior to the phototactic assays, all tested fish were subjected to a period of at least 8 minutes  
486 of habituation under whole-field illumination at an intensity of  $I_{max} = 450\mu W.cm^{-2}$ . For both  
487 paradigms, the absolute orientation of the virtual source was randomly selected when initiating a  
488 new experimental sequence (each time the animal would re-enter the region of interest). Thus the  
489 relative orientation of the fish towards the light source  $\theta_n$  was calculated online using the absolute  
490 orientation of the fish  $\alpha_n$  and the randomly chosen orientation of the source  $\alpha_{source}$ :  $\theta_n = \alpha_n - \alpha_{source}$ .

491 Lateralized paradigm. A circle of 6cm in diameter was projected under and centered on the fish.  
492 The circle was divided into two parts, covering the left and right side of the fish. The separation  
493 between the two parts corresponded to the animal midline. The division (2mm thick) as well as a  
494 triangle ( $30^\circ$ ) in front of the head were darkened to avoid interception of intensity coming from the  
495 right side of the fish by its left eye and *vice-versa*. Left and right intensities ( $I_L$  and  $I_R$ ) were varied  
496 linearly as a function of  $\theta$ , such that  $I_L + I_R = I$ ,  $I$  being constant. Since during the habituation  
497 period, the whole arena was lit, the intensity received by the fish drops by a factor of 2 with the  
498 establishment of the circle, at the beginning of the trial. Note that when heading towards the virtual  
499 light source, the total intensity received on both eyes is equal to half the value  $I_{max}$  that the animal  
500 experiences during the conditioning phase. Although our imposed contrast profiles displays two  
501 angles for which the contrast is null, namely  $\theta = 0$  and  $\pi$ , only does the first one correspond to a  
502 stable equilibrium point. When  $\theta$  is close to zero, any excursion away from this particular direction  
503 results in a contrast that drives the animal back to the null angle. Conversely, when  $\theta \approx \pi$ , the  
504 contrast drives the animal away from  $\pi$  (unstable equilibrium).

505 Temporal paradigm. The whole arena was illuminated with an intensity locked onto the fish  
506 orientation  $\theta_n$  relative to a virtual light source. The initial orientation was randomly chosen at the  
507 beginning of a recording sequence. Three different intensity angular profiles were implemented:  
508 (uniform 1) a sinusoidal profile, with a maximum intensity of 60% of  $I_{max}$ , (uniform 2) an exponential  
509 profile, with a maximum intensity of 60% of  $I_{max}$  and finally (uniform 3) an exponential profile with a  
510 maximum intensity of 30% of  $I_{max}$ .

## 511 Data analysis

512 Data analysis was performed using a custom-written code in Matlab. When representing the mean  
513 of a variable against another, bin edges were chosen such that each bin would encompass the  
514 same number of elements. Circular statistics analyses (mean, variance, uniformity) and circular  
515 statistics tests, namely the circular Rayleigh test of non-uniformity of data and the one-sample  
516 test for the mean angle of a circular distribution (tested on the orientation of the light virtual light  
517 source  $\langle \theta \rangle = 0$ ) were performed using CircStat toolbox for Matlab (*Berens, 2009*).

518 In order to calculate the mean resultant vector length  $\mathbf{R}$ , we consider all the angular positions  $\theta_n$   
519 relative to the source. The resultant vector is defined, in the complex plane, as  $\mathbf{v} = \frac{1}{N} \sum \exp i\theta_n$  and  
520 its length as  $\mathbf{R} = |\mathbf{v}|$ . In order to assess to what extent a distribution is biased towards a specific  
521 direction (here, the light source), the quantity  $\mathbf{R} \cos(\theta)$  was sometimes used : the mean resultant  
522 vector projected onto the direction of the light source.

523  
524 Individual fish often exhibit a consistent (minute) bias towards one direction (either leftward  
525 or rightward). This bias was subtracted before performing the different analyses, in order to  
526 guarantee that  $\langle \alpha \rangle = 0$  in the absence of a stimulus. The distribution of reorientation angles  $\delta\theta_n$   
527 during spontaneous swimming periods was fitted with a constrained double-Gaussian function.  
528 We imposed that both the mean absolute angle and variance of the fitting function be consistent  
529 with the experimental measurements. This yields an expression with only one independent fitting  
530 parameter  $p_{turn}$  in the form:

$$f(x) = \frac{1}{\sqrt{2\pi}} \left( \frac{p_{turn}}{\sigma_{turn}} e^{-\frac{1}{2} \left( \frac{x}{\sigma_{turn}} \right)^2} + \frac{1-p_{turn}}{\sigma_f} e^{-\frac{1}{2} \left( \frac{x}{\sigma_{fwd}} \right)^2} \right) \quad (1)$$

531 using

$$\sigma_{turn} = \frac{\mu_{abs} p_{turn} + \sqrt{\mu_{abs}^2 p_{turn}^2 - [\mu_{abs}^2 - V(1-p_{turn})] [p_{turn}^2 + p_{turn}(1-p_{turn})]}}{p_{turn}^2 + p_{turn}(1-p_{turn})}$$

and

$$\sigma_{fwd} = \frac{\mu_{abs} \sqrt{\pi/2} - p_{turn} \sigma_{turn}}{1-p_{turn}}$$

with

$$\mu_{abs} = \langle |\delta\theta| \rangle, V = \langle \delta\theta^2 \rangle$$

532 To evaluate the mean and variance of the forward and turn bouts under various visual context,  
533 the distributions in different bins were also fitted with a constrained double Gaussian model as in  
534 (1). The stereovisual data distributions were fitted with two additional mean terms  $\mu_{turn}$  and  $\mu_{fwd}$  ;  
535 and for the klinotaxis assay, with a constraint on  $\sigma_{fwd}$  and  $\mu_{fwd}$ . The bins were constructed either on  
536 the contrast  $c$  experienced just before bout  $n$  or on the relative difference of intensity experienced  
537 at bout  $n-1$  :  $\delta I / I = 2 \frac{I_{n-1} - I_{n-2}}{I_{n-1} + I_{n-2}}$ .

538 All distributions of  $\theta_n$  and analyses of bias were computed using trajectories from bouts number  
539 2 to a maximum of the median number of bouts per sequence in each type of experiment. The  
540 median number of bouts in each experiment was  $med_{stereo} = 17$  for the tropotaxis experiment, and  
541 27, 15, 17 for the klinotaxis assays for the 3 profiles 1-3, respectively.

## 543 Numerical simulations

544 The random walk model simulations were performed using a custom-written code in MATLAB. Initial  
545 orientations and positions within the ROI were randomly sampled from, respectively, a uniform  
546 distribution and a normal distribution centered on a circle of radius 20 mm from the center of the  
547 ROI and a standard deviation of 1.3 mm (mimicking the starting points of experimental data).

548 At each step, the walker draws a certain angular step-size from the data: either from the turning  
549 distribution with a probability  $p_{turn}$  or from the forward distribution with a probability  $1 - p_{turn}$ .  
550 Respective means are  $\mu_{turn}$  and  $\mu_{fwd}$  and standard deviation  $\sigma_{turn}$  and  $\sigma_{fwd}$ . The direction of only  
551 the turns is set by the probability of flipping sides  $p_{flip}$ . For the spatially constrained simulations,  
552 the walker also draws a distance step-size (between two successive positions) from two different  
553 gamma distributions : one for the turning bouts, a second one for the scoots. Under neutral  
554 conditions (uniform illumination), all parameters are constant.  
555 For simulation of stereovisual phototactic conditions, only  $p_{flip}$  changes linearly as a function of the  
556 contrast (based on the data represented in **Figure 2J**).  
557 As for the temporal phototaxis, parameters  $p_{turn}$  and  $\sigma_{turn}$  were adapted as a function of the relative  
558 illumination change  $\delta I/I$  experienced at the previous steps (as represented in **Figure 3G-H**).  
559 The simulations also account for the adaptation illumination preceding an experimental trial, prior  
560 the first bout.

## 561 Competing interests

562 The authors declare no competing interests.

## 563 References

- 564 **Adler J**, Tso WW. "Decision"-Making in Bacteria : Chemotactic Response of Escherichia coli to Conflicting Stimuli.  
565 American Association for the Advancement of Science. 1974; 184(4143):1292–1294.
- 566 **Ahrens MB**, Orger MB, Robson DN, Li JM, Keller PJ. Whole-brain functional imaging at cellular resolution using  
567 light-sheet microscopy. Nature Methods. 2013; 10(5):413–420. doi: [10.1038/nmeth.2434](https://doi.org/10.1038/nmeth.2434).
- 568 **Berens P**. CircStat: A MATLAB Toolbox for Circular Statistics. Journal of Statistical Software. 2009; 1(1):128–129.  
569 doi: [10.1002/wics.10](https://doi.org/10.1002/wics.10).
- 570 **Berg HC**, Brown DA. Chemotaxis in E coli analysed by 3D tracking. Nature. 1972; 239:500–504.
- 571 **Bianco IH**, Engert F. Visuomotor transformations underlying hunting behavior in zebrafish. Current Biology.  
572 2015; 25(7):831–846. doi: [10.1016/j.cub.2015.01.042](https://doi.org/10.1016/j.cub.2015.01.042).
- 573 **Bianco IH**, Kampff AR, Engert F. Prey capture behavior evoked by simple visual stimuli in larval zebrafish.  
574 Frontiers in Systems Neuroscience. 2011; 5(December 2011):1–13. doi: [10.3389/fnsys.2011.00101](https://doi.org/10.3389/fnsys.2011.00101).
- 575 **Brunel N**, Wang XJ. Effects of Neuromodulation in a Cortical Network Model of Object Working Memory  
576 Dominated by Recurrent Inhibition. Journal of computational neuroscience. 2001 02; 11:63–85. doi:  
577 [10.1023/A:1011204814320](https://doi.org/10.1023/A:1011204814320).
- 578 **Budick Sa**, O'Malley DM. Locomotor repertoire of the larval zebrafish: swimming, turning and prey capture.  
579 The Journal of experimental biology. 2000; 203(Pt 17):2565–79. doi: [10.1242/jeb.01529](https://doi.org/10.1242/jeb.01529).
- 580 **Burgess HA**, Granato M. Modulation of locomotor activity in larval zebrafish during light adaptation. Journal of  
581 Experimental Biology. 2007; 210(14):2526–2539. doi: [10.1242/jeb.003939](https://doi.org/10.1242/jeb.003939).
- 582 **Burgess H**, Schoch H, Granato M. Distinct retinal pathways drive spatial orientation behaviors in zebrafish  
583 navigation. Current Biology. 2010; 6(8):381–386. doi: [10.1021/nn300902w.Release](https://doi.org/10.1021/nn300902w.Release).
- 584 **Celani A**, Vergassola M. Bacterial strategies for chemotaxis response. Proceedings of the National Academy of  
585 Sciences. 2010; 107(4):1391–1396. doi: [10.1073/pnas.0909673107](https://doi.org/10.1073/pnas.0909673107).
- 586 **Chen X**, Engert F. Navigational strategies underlying phototaxis in larval zebrafish. Frontiers in Systems  
587 Neuroscience. 2014; 8(March):1–13. doi: [10.3389/fnsys.2014.00039](https://doi.org/10.3389/fnsys.2014.00039).
- 588 **Dunn TW**, Mu Y, Narayan S, Randlett O, Naumann EA, Yang CT, Schier AF, Freeman J, Engert F, Ahrens MB.  
589 Brain-wide mapping of neural activity controlling zebrafish exploratory locomotion. eLife. 2016; 5(March  
590 2016):1–29. doi: [10.7554/eLife.12741](https://doi.org/10.7554/eLife.12741).
- 591 **Emran F**, Rihel J, Adolph AR, Dowling JE. Zebrafish larvae lose vision at night. Proceedings of the National  
592 Academy of Sciences. 2009; 107(13):6034–6039. doi: [10.1073/pnas.0914718107](https://doi.org/10.1073/pnas.0914718107).

- 593 **Emran F**, Rihel J, Adolph AR, Wong KY, Kraves S, Dowling JE. OFF ganglion cells cannot drive the optokinetic  
594 reflex in zebrafish. *Proceedings of the National Academy of Sciences*. 2007; 104(48):19126–19131.
- 595 **Fechner GT**. *Elemente der Psychophysik*; 1860.
- 596 **Fernandes AM**, Fero K, Arrenberg AB, Bergeron SA, Driever W, Burgess HA. Deep brain photorecep-  
597 tors control light seeking behavior in zebrafish larvae. *Current Biology*. 2013; 22(21):2042–2047. doi:  
598 [10.1016/j.cub.2012.08.016](https://doi.org/10.1016/j.cub.2012.08.016).Deep.
- 599 **Fiser J**, Chiu C, Weliky M. Small modulation of ongoing cortical dynamics by sensory input during natural vision.  
600 *Nature*. 2004; 431(7008):573–578. doi: 10.1038/nature02907.
- 601 **Fraenkel GS**, Gunn DL. *The Orientation of Animals, Kinesis, Taxes and Compass Reactions*; 1961. doi:  
602 [10.1093/aesa/34.3.690a](https://doi.org/10.1093/aesa/34.3.690a).
- 603 **Freeman W**. The Hebbian paradigm reintegrated: Local reverberations as internal representations. *Behavioral*  
604 *and Brain Sciences*. 1995 12; 18:631 – 631. doi: 10.1017/S0140525X0004022X.
- 605 **Girdhar K**, Gruebele M, Chemla YR. The behavioral space of zebrafish locomotion and its neural network analog.  
606 *PLoS ONE*. 2015; 10(7):1–18. doi: [10.1371/journal.pone.0128668](https://doi.org/10.1371/journal.pone.0128668).
- 607 **Gomez-Marin A**, Louis M. Active sensation during orientation behavior in the *Drosophila* larva: more sense than  
608 luck. *Current Opinion in Neurobiology*. 2012; 22(2):208 – 215. doi: <https://doi.org/10.1016/j.conb.2011.11.008>,  
609 neuroethology.
- 610 **Gomez-Marin A**, Stephens GJ, Louis M. Active sampling and decision making in *Drosophila* chemotaxis. *Nature*  
611 *Communications*. 2011; 2(1):410–441. doi: 10.1038/ncomms1455.
- 612 **Horstick EJ**, Bayleyen Y, Sinclair JL, Burgess HA. Search strategy is regulated by somatostatin signaling and deep  
613 brain photoreceptors in zebrafish. *BMC Biology*. 2017; 15(1):1–16. doi: 10.1186/s12915-016-0346-2.
- 614 **Humberg TH**, Bruegger P, Afonso B, Zlatic M, Truman JW, Gershow M, Samuel A, Sprecher SG. Dedicated  
615 photoreceptor pathways in *Drosophila* larvae mediate navigation by processing either spatial or temporal  
616 cues. *Nature Communications*. 2018; 9(1):1–16. doi: 10.1038/s41467-018-03520-5.
- 617 **Johnson RE**, Linderman S, Panier T, Wee CL, Song E, Herrera KJ, Miller A, Engert F. Probabilistic Models of Larval  
618 Zebrafish Behavior: Structure on Many Scales. *bioRxiv*. 2019; p. 672246. doi: 10.1101/672246.
- 619 **Kane EA**, Gershow M, Afonso B, Larderet I, Klein M, Carter AR, de Bivort BL, Sprecher SG, Samuel ADT. Senso-  
620 rimotor structure of *Drosophila* larva phototaxis. *Proceedings of the National Academy of Sciences*. 2013;  
621 110(40):E3868–E3877. doi: [10.1073/pnas.1215295110](https://doi.org/10.1073/pnas.1215295110).
- 622 **Liu Y**, Carmer R, Zhang G, Venkatraman P, Brown SA, Pang CP, Zhang M, Ma P, Leung YF. Statistical analysis of  
623 zebrafish locomotor response. *PLoS ONE*. 2015; 10(10):1–25. doi: [10.1371/journal.pone.0139521](https://doi.org/10.1371/journal.pone.0139521).
- 624 **Lovely PS**, Dahlquist FW. Statistical Measures of Bacterial Motility. *J theor Biol*. 1975; p. 477–496.
- 625 **Macnab RM**, Koshland DE. The Gradient-Sensing Mechanism in Bacterial Chemotaxis. *Proceedings of the*  
626 *National Academy of Sciences*. 1972; 69(9):2509–2512. doi: [10.1073/pnas.69.9.2509](https://doi.org/10.1073/pnas.69.9.2509).
- 627 **Marée AFM**, Panfilov AV, Hogeweg P. Phototaxis during the slug stage of *Dictyostelium discoideum*: A  
628 model study. *Proceedings of the Royal Society B: Biological Sciences*. 1999; 266(1426):1351–1360. doi:  
629 [10.1098/rspb.1999.0787](https://doi.org/10.1098/rspb.1999.0787).
- 630 **Marques JC**, Lackner S, Félix R, Orger MB. Structure of the Zebrafish Locomotor Repertoire Revealed with  
631 Unsupervised Behavioral Clustering. *Current Biology*. 2018; p. 181–195. doi: [10.1016/j.cub.2017.12.002](https://doi.org/10.1016/j.cub.2017.12.002).
- 632 **Matsuo Y**, Uozumi N, Matsuo R. Photo-tropotaxis based on projection through the cerebral commissure in the  
633 terrestrial slug *Limax*. *Journal of Comparative Physiology A: Neuroethology, Sensory, Neural, and Behavioral*  
634 *Physiology*. 2014; 200(12):1023–1032. doi: 10.1007/s00359-014-0954-7.
- 635 **Maximino C**, Brito TM, Moraes FD, Oliveira FVC, Taccolini IB, Pereira PM, Colmanetti R, Lozano R, Gazolla RA,  
636 Rodrigues STK, Oliveira Coelho Lameirão SV, Pontes AAA, Romão CF, Prado VM, Gouveia jr A. A Comparative  
637 Analysis of the Preference for Dark Environments in Five Teleosts. *International Journal of Comparative*  
638 *Psychology*. 2007; 20(4):351–367.
- 639 **McClenahan P**, Troup M, Scott EK. Fin-tail coordination during escape and predatory behavior in larval zebrafish.  
640 *PLoS ONE*. 2012; 7(2):1–11. doi: [10.1371/journal.pone.0032295](https://doi.org/10.1371/journal.pone.0032295).

- 641 **Mello BA**, Tu Y. Effects of adaptation in maintaining high sensitivity over a wide range of backgrounds for  
642 *Escherichia coli* chemotaxis. *Biophysical Journal*. 2007; 92(7):2329–2337. doi: [10.1529/biophysj.106.097808](https://doi.org/10.1529/biophysj.106.097808).
- 643 **Miller AC**, Thiele TR, Faumont S, Moravec ML, Lockery SR. Step-Response Analysis of Chemotaxis in *Caenorhab-*  
644 *ditis elegans*. *Journal of Neuroscience*. 2005; 25(13):3369–3378. doi: [10.1523/JNEUROSCI.5133-04.2005](https://doi.org/10.1523/JNEUROSCI.5133-04.2005).
- 645 **Oliveira NM**, Foster KR, Durham WM. Single-cell twitching chemotaxis in developing biofilms. *Proceedings of*  
646 *the National Academy of Sciences*. 2016; 113(23):6532–6537. doi: [10.1073/pnas.1600760113](https://doi.org/10.1073/pnas.1600760113).
- 647 **Orger M**, Baier H. Channeling of red and green cone inputs to the zebrafish optomotor response. *Visual*  
648 *Neuroscience*. 2005; 22(3):275–281. doi: [10.1017/s0952523805223039](https://doi.org/10.1017/s0952523805223039).
- 649 **Panier T**, Romano SA, Olive R, Pietri T, Sumbre G, Candelier R, Debrégeas G. Fast functional imaging of multiple  
650 brain regions in intact zebrafish larvae using Selective Plane Illumination Microscopy. *Frontiers in Neural*  
651 *Circuits*. 2013; 7(April):1–11. doi: [10.3389/fncir.2013.00065](https://doi.org/10.3389/fncir.2013.00065).
- 652 **Prober DA**, Rihel J, Onah AA, Sung RJ, Schier AF. Hypocretin/Orexin Overexpression Induces An Insomnia-Like  
653 Phenotype in Zebrafish. *Journal of Neuroscience*. 2006; 26(51):13400–13410. doi: [10.1523/JNEUROSCI.4332-06.2006](https://doi.org/10.1523/JNEUROSCI.4332-06.2006).
- 655 **Sawin EP**, Harris LR, Campos AR, Sokolowski MB. Sensorimotor transformation from light reception to photo-  
656 tactic behavior in *Drosophila* larvae (Diptera: Drosophilidae). *Journal of Insect Behavior*. 1994; 7(4):553–567.  
657 doi: [10.1007/BF02025449](https://doi.org/10.1007/BF02025449).
- 658 **Serra EL**, Medalha CC, Mattioli R. Natural preference of zebrafish (*Danio rerio*) for a dark environment. *Brazilian*  
659 *Journal of Medical and Biological Research*. 1999; 32(12):1551–1553. doi: [10.1590/S0100-879X1999001200016](https://doi.org/10.1590/S0100-879X1999001200016).
- 660 **Shadlen MN**, Newsome WT. Motion perception: Seeing and deciding. *Proceedings of the National Academy of*  
661 *Sciences of the United States of America*. 1996; 93(2):628–633. doi: [10.1073/pnas.93.2.628](https://doi.org/10.1073/pnas.93.2.628).
- 662 **Shadlen MN**, Newsome WT. Neural basis of a perceptual decision in the parietal cortex (area LIP) of the rhesus  
663 monkey. *Journal of Neurophysiology*. 2001; 86(4):1916–1936. doi: [10.1152/jn.2001.86.4.1916](https://doi.org/10.1152/jn.2001.86.4.1916).
- 664 **Stephen S Easter J**, Nicola GN. The Development of Vision in the Zebrafish (*Danio rerio*). *Developmental Biology*.  
665 1996; 180(2):646 – 663. doi: <https://doi.org/10.1006/dbio.1996.0335>.
- 666 **Tastekin I**, Khandelwal A, Tadres D, Fessner ND, Truman JW, Zlatic M, Cardona A, Louis M. Sensorimotor pathway  
667 controlling stopping behavior during chemotaxis in the *Drosophila melanogaster* larva. *Elife*. 2018; 7:e38740.
- 668 **Tsodyks AM**, Kenet T, Grinvald A, Arieli A, Tsodyks M, Kenet T, Grinvald A, Arieli A. Linking Spontaneous Activity  
669 of Single Cortical Neurons and the Underlying Functional Architecture. *Science*. 1999; 286(5446):1943–1946.
- 670 **Uhlenbeck GE**, Ornstein LS. On the Theory of the Brownian Motion. *Phys Rev*. 1930 Sep; 36:823–841. doi:  
671 [10.1103/PhysRev.36.823](https://doi.org/10.1103/PhysRev.36.823).
- 672 **Wang XJ**. Synaptic reverberation underlying mnemonic persistent activity. *Trends in neurosciences*. 2001 09;  
673 24:455–63. doi: [10.1016/S0166-2236\(00\)01868-3](https://doi.org/10.1016/S0166-2236(00)01868-3).
- 674 **Wang XJ**. Probabilistic Decision Making by Slow Reverberation in Cortical Circuits. *Neuron*. 2002; 36(5):955 –  
675 968. doi: [https://doi.org/10.1016/S0896-6273\(02\)01092-9](https://doi.org/10.1016/S0896-6273(02)01092-9).
- 676 **Wang X**. Decision Making in Recurrent Neuronal Circuits. *Neuron*. 2008; 60(2):215–234. doi:  
677 [10.1016/j.neuron.2008.09.034](https://doi.org/10.1016/j.neuron.2008.09.034).Decision.
- 678 **Ward A**, Liu J, Feng Z, Xu XZS. Light-sensitive neurons and channels mediate phototaxis in *C. elegans*. *Nature*  
679 *Neuroscience*. 2008 07; 11:916 EP –. doi: <https://doi.org/10.1038/nn.2155>.
- 680 **Ward S**. Chemotaxis by the Nematode *Caenorhabditis elegans*: Identification of Attractants and Analysis of the  
681 Response by Use of Mutants. *Proceedings of the National Academy of Sciences*. 1973; 70(3):817–821. doi:  
682 [10.1073/pnas.70.3.817](https://doi.org/10.1073/pnas.70.3.817).
- 683 **Wolf S**, Dubreuil AM, Bertoni T, Böhm UL, Bormuth V, Candelier R, Karpenko S, Hildebrand DGC, Bianco  
684 IH, Monasson R, Debrégeas G. Sensorimotor computation underlying phototaxis in zebrafish. *Nature*  
685 *Communications*. 2017; 8(1):1–12. doi: [10.1038/s41467-017-00310-3](https://doi.org/10.1038/s41467-017-00310-3).
- 686 **Yuan J**, Fahrner KA, Turner L, Berg HC. Asymmetry in the clockwise and counterclockwise rotation of the  
687 bacterial flagellar motor. *Proceedings of the National Academy of Sciences*. 2010; 107(29):12846–12849. doi:  
688 [10.1073/pnas.1007333107](https://doi.org/10.1073/pnas.1007333107).

## 689 Appendix 1

### 690 Modelling spontaneous navigation of zebrafish larvae

691 We model the discrete trajectories (sequences of bouts) as a stochastic process using two  
 692 independent Markov chains, depicted in **Figure 1E**. The *bout type* chain (top) controls the  
 693 alternation between forward and turning bouts, with possible states  $F_n$  and  $T_n$  at time  $n$ , while  
 694 the *side* chain (bottom) controls the left/right orientations of turning bouts, with possible  
 695 states  $L_n$  and  $R_n$ . All possible states are combinations of the states of the two chains, namely  
 696  $\{FL\}_n$ ,  $\{FR\}_n$ ,  $\{TL\}_n$ , and  $\{TR\}_n$ . The transition rates of the bout type chain are  $k_{F \rightarrow T}$  and  
 697  $k_{T \rightarrow F}$ , where  $k_{F \rightarrow T}/k_{T \rightarrow F} = p_{turn}$  is the overall fraction of turning bouts. For the side chain,  
 698 under constant uniform illumination, the right and left states are equiprobable, and the two  
 699 transition probabilities are thus equal:  $k_{R \rightarrow L} = k_{L \rightarrow R} = p_{flip}$ .

700 The two chains operate synchronously: at every time step transitions on both chains are  
 701 triggered simultaneously, and a reorientation value  $\delta\alpha_n$  is drawn based on the resulting state.  
 702 When the fish is in a turning state,  $\{TL\}_n$  or  $\{TR\}_n$ , the reorientation angle is sampled from  
 703 the positive and negative side of a centered normal distribution with standard deviation  $\sigma_{turn}$   
 704 for left and right turns, respectively. When the fish is in a forward state,  $\{FL\}_n$  or  $\{FR\}_n$ ,  
 705 the reorientation angle is drawn from a normal distribution with standard deviation  $\sigma_{fwd}$ .  
 706 Therefore, for forward bouts the resulting  $\delta\alpha_n$  can be positive or negative, irrespective of the  
 707 left/right state of the side chain. Altogether, the general statistical distribution of turning  
 708 amplitudes  $\delta\alpha_n$  used in **Figure 1F** reads

$$714 P(\delta\alpha_n) = \phi_t(\delta\alpha_n) + \phi_f(\delta\alpha_n) \quad (A1)$$

715 with

$$716 \phi_t = p_{turn} \mathcal{N}(0, \sigma_{turn}^2) \quad \text{and} \quad \phi_f = (1 - p_{turn}) \mathcal{N}(0, \sigma_{fwd}^2) \quad (A2)$$

### 718 Mean amplitude at $n + 1$

719 Within this framework, one can analytically compute the mean square angle at time  $n + 1$ , as  
 720 detailed below:  
 721  
 722

$$723 \langle \delta\alpha_{n+1}^2 \rangle = \mathbb{P}(F_{n+1})\sigma_{fwd}^2 + \mathbb{P}(T_{n+1})\sigma_{turn}^2 \quad (A3)$$

724  
 725  
 726 The two probabilities read:

$$727 \mathbb{P}(F_{n+1}) = \mathbb{P}(F_n)(1 - k_{F \rightarrow T}) + \mathbb{P}(T_n)k_{T \rightarrow F}$$

$$728 \mathbb{P}(T_{n+1}) = \mathbb{P}(T_n)(1 - k_{T \rightarrow F}) + \mathbb{P}(F_n)k_{F \rightarrow T}$$

729 such that

$$730 \langle \delta\alpha_{n+1}^2 \rangle = \mathbb{P}(F_n) \left[ \sigma_{fwd}^2 + k_{F \rightarrow T}(\sigma_{turn}^2 - \sigma_{fwd}^2) \right] + \mathbb{P}(T_n) \left[ \sigma_{turn}^2 + k_{T \rightarrow F}(\sigma_{fwd}^2 - \sigma_{turn}^2) \right]$$

731 Using the functions defined in A2 we introduce the function  $f(\delta\alpha_n)$ :

$$732 f(\delta\alpha_n) = \mathbb{P}(T_n | \delta\alpha_n) = \frac{\phi_t(\delta\alpha_n)}{\phi_t(\delta\alpha_n) + \phi_f(\delta\alpha_n)} \quad (A4)$$

733 The mean square amplitude at time  $n + 1$  can thus be written, as a function of  $\delta\alpha_n$  as:

$$734 \langle \delta\alpha_{n+1}^2 \rangle = \sigma_{fwd}^2 + k_{F \rightarrow T}(\sigma_{turn}^2 - \sigma_{fwd}^2) + f(|\delta\alpha_n|)(\sigma_{turn}^2 - \sigma_{fwd}^2)(1 - k_{T \rightarrow F} - k_{F \rightarrow T}) \quad (A5)$$

757  
758  
759  
760  
761  
762  
763  
764  
765  
766  
767  
768  
769  
770  
771  
772  
773  
774  
775  
776  
777  
778  
779  
780  
781  
782  
783  
784  
785  
786  
787  
788  
789  
790  
791  
792  
793  
794  
795  
796  
797  
798  
799  
800  
801  
802  
803

This expression is used to fit the data in **Figure 2G** and estimate the two transition rates. These are found to be close to the ratio of turning and forward bouts, *i.e.*  $k_{F \rightarrow T}/p_{turn} = k_{T \rightarrow F}/(1 - p_{turn}) \approx 0.8$ . In the following, we set  $k_{F \rightarrow T} = p_{turn}$  and  $k_{T \rightarrow F} = 1 - p_{turn}$ , thus ignoring the weak memory component in the selection of turning vs forward bouts.

### Mean reorientation at $n + 1$

Similarly, one can compute the theoretical expression of the mean reorientation angle at time  $n + 1$ :

$$\langle \delta\alpha_{n+1} \rangle = \mathbb{P}(\{FL\}_{n+1})\mu_f + \mathbb{P}(\{FR\}_{n+1})\mu_f + \mathbb{P}(\{TL\}_{n+1})\mu_L + \mathbb{P}(\{TR\}_{n+1})\mu_R \quad (A6)$$

with

$$\mu_f = 0 \quad \text{and} \quad \mu_L = -\mu_R = \sqrt{\frac{2}{\pi}}\sigma_{turn} \quad (A7)$$

Then:

$$\mathbb{P}(\{TL\}_{n+1}) = \mathbb{P}(T_{n+1})\mathbb{P}(L_{n+1}) = p_{turn} [p_{flip}\mathbb{P}(R_n) + (1 - p_{flip})\mathbb{P}(L_n)]$$

$$\mathbb{P}(\{TR\}_{n+1}) = \mathbb{P}(T_{n+1})\mathbb{P}(R_{n+1}) = p_{turn} [p_{flip}\mathbb{P}(L_n) + (1 - p_{flip})\mathbb{P}(R_n)]$$

and

$$\langle \delta\alpha_{n+1} \rangle = p_{turn}(1 - 2p_{flip})\sqrt{\frac{2}{\pi}}\sigma_{turn} [\mathbb{P}(L_n) - \mathbb{P}(R_n)] \quad (A8)$$

Without further assumption, this simply confirms  $\langle \delta\alpha_{n+1} \rangle = 0$ . Given the reorientation at time  $n$ , this expression now writes:

$$\langle \delta\alpha_{n+1} \rangle_{|\delta\alpha_n} = p_{turn}(1 - 2p_{flip})\sqrt{\frac{2}{\pi}}\sigma_{turn} [\mathbb{P}(L_n|\delta\alpha_n) - \mathbb{P}(R_n|\delta\alpha_n)] \quad (A9)$$

Since

$$\mathbb{P}(L_n|\delta\alpha_n) = \mathbb{P}(L_n|T_n, \delta\alpha_n)\mathbb{P}(T_n|\delta\alpha_n) + \mathbb{P}(L_n|F_n, \delta\alpha_n)\mathbb{P}(F_n|\delta\alpha_n)$$

$$\mathbb{P}(R_n|\delta\alpha_n) = \mathbb{P}(R_n|T_n, \delta\alpha_n)\mathbb{P}(T_n|\delta\alpha_n) + \mathbb{P}(R_n|F_n, \delta\alpha_n)\mathbb{P}(F_n|\delta\alpha_n)$$

and

$$\mathbb{P}(L_n|F_n, \delta\alpha_n) = \mathbb{P}(R_n|F_n, \delta\alpha_n) = 1/2$$

we obtain

$$\langle \delta\alpha_{n+1} \rangle_{|\delta\alpha_n} = [\mathbb{P}(L_n|T_n, \delta\alpha_n) - \mathbb{P}(R_n|T_n, \delta\alpha_n)] p_{turn}(1 - 2p_{flip})\sqrt{\frac{2}{\pi}}\sigma_{turn}f(\delta\alpha_n) \quad (A10)$$

Then, noting that

$$\begin{cases} \mathbb{P}(L_n|T_n, \delta\alpha_n > 0) = 1 \\ \mathbb{P}(R_n|T_n, \delta\alpha_n > 0) = 0 \end{cases} \quad \text{and} \quad \begin{cases} \mathbb{P}(L_n|T_n, \delta\alpha_n < 0) = 0 \\ \mathbb{P}(R_n|T_n, \delta\alpha_n < 0) = 1 \end{cases}$$

we finally obtain the formula used to fit the data in **Figure 1G**:

$$\langle \delta\alpha_{n+1} \rangle_{|\delta\alpha_n} = \text{sgn}(\delta\alpha_n)\sqrt{\frac{2}{\pi}}p_{turn}(1 - 2p_{flip})\sigma_{turn}f(\delta\alpha_n) \quad (A11)$$

804

## Autocorrelation of the reorientations

One can then compute the correlation of reorientation amplitudes, defined for  $q \in \mathbb{N}^*$  as:

$$C_q = \frac{\langle \delta\alpha_n \delta\alpha_{n+q} \rangle - \langle \delta\alpha_n \rangle \langle \delta\alpha_{n+q} \rangle}{\sqrt{\langle \delta\alpha_n^2 \rangle} \sqrt{\langle \delta\alpha_{n+q}^2 \rangle}} = \frac{\langle \delta\alpha_n \delta\alpha_{n+q} \rangle}{\langle \delta\alpha_n^2 \rangle} \quad (\text{A12})$$

with the normalization coefficient equal to the variance of reorientations

$$\langle \delta\alpha_n^2 \rangle = p_{turn} \sigma_{turn}^2 + (1 - p_{turn}) \sigma_{fwd}^2 \quad (\text{A13})$$

The term  $\langle \delta\alpha_n \delta\alpha_{n+q} \rangle$  can be computed in a similar manner as for equation A6, but with more terms corresponding to the 16 possible combinations of states:

$$\begin{array}{cccc} \{FL\}_n, \{FL\}_{n+q} & \{FL\}_n, \{FR\}_{n+q} & \{FL\}_n, \{TL\}_{n+q} & \{FL\}_n, \{TR\}_{n+q} \\ \{FR\}_n, \{FL\}_{n+q} & \{FR\}_n, \{FR\}_{n+q} & \{FR\}_n, \{TL\}_{n+q} & \{FR\}_n, \{TR\}_{n+q} \\ \{TL\}_n, \{FL\}_{n+q} & \{TL\}_n, \{FR\}_{n+q} & \{TL\}_n, \{TL\}_{n+q} & \{TL\}_n, \{TR\}_{n+q} \\ \{TR\}_n, \{FL\}_{n+q} & \{TR\}_n, \{FR\}_{n+q} & \{TR\}_n, \{TL\}_{n+q} & \{TR\}_n, \{TR\}_{n+q} \end{array}$$

Only the 4 states in the bottom-right corner have a finite contribution, since all the others terms are multiplied by  $\mu_f = 0$ . Thus:

$$\begin{aligned} \langle \delta\alpha_n \delta\alpha_{n+q} \rangle &= \mathbb{P}(\{TL\}_n, \{TL\}_{n+q}) \mu_L^2 + \mathbb{P}(\{TL\}_n, \{TR\}_{n+q}) \mu_L \mu_R + \\ &\quad \mathbb{P}(\{TR\}_n, \{TL\}_{n+q}) \mu_R \mu_L + \mathbb{P}(\{TR\}_n, \{TR\}_{n+q}) \mu_R^2 \end{aligned}$$

and, using A7 and

$$\begin{aligned} \mathbb{P}(\{TL\}_n, \{TL\}_{n+q}) &= \mathbb{P}(T_n) \mathbb{P}(T_{n+q}) \mathbb{P}(L_n) \mathbb{P}(L_{n+q} | L_n) = \frac{p_{turn}^2}{2} \mathbb{P}(L_{n+q} | L_n) \\ \mathbb{P}(\{TL\}_n, \{TR\}_{n+q}) &= \mathbb{P}(T_n) \mathbb{P}(T_{n+q}) \mathbb{P}(L_n) \mathbb{P}(R_{n+q} | L_n) = \frac{p_{turn}^2}{2} \mathbb{P}(R_{n+q} | L_n) \\ \mathbb{P}(\{TR\}_n, \{TL\}_{n+q}) &= \mathbb{P}(T_n) \mathbb{P}(T_{n+q}) \mathbb{P}(R_n) \mathbb{P}(L_{n+q} | R_n) = \frac{p_{turn}^2}{2} \mathbb{P}(L_{n+q} | R_n) \\ \mathbb{P}(\{TR\}_n, \{TR\}_{n+q}) &= \mathbb{P}(T_n) \mathbb{P}(T_{n+q}) \mathbb{P}(R_n) \mathbb{P}(R_{n+q} | R_n) = \frac{p_{turn}^2}{2} \mathbb{P}(R_{n+q} | R_n) \end{aligned}$$

and noting that

$$\begin{aligned} \mathbb{P}(L_{n+q} | L_n) &= \mathbb{P}(R_{n+q} | R_n) = \sum_{\substack{i=1 \\ i \text{ odd}}}^{q+1} \binom{q}{i} p_{flip}^{i-1} (1 - p_{flip})^{q-i+1} \\ \mathbb{P}(L_{n+q} | R_n) &= \mathbb{P}(R_{n+q} | L_n) = \sum_{\substack{i=1 \\ i \text{ even}}}^{q+1} \binom{q}{i} p_{flip}^{i-1} (1 - p_{flip})^{q-i+1} \end{aligned}$$

one obtains

$$\langle \delta\alpha_n \delta\alpha_{n+q} \rangle = p_{turn}^2 \left[ \sum_{i=1}^{q+1} (-1)^{q+1} \binom{q}{i} p_{flip}^{i-1} (1 - p_{flip})^{q-i+1} \right] \mu_L^2 = \frac{2}{\pi} (1 - 2p_{flip})^q p_{turn}^2 \sigma_{turn}^2$$

and finally:

$$C_q = \frac{2}{\pi} \frac{p_{turn}^2 \sigma_{turn}^2}{p_{turn} \sigma_{turn}^2 + (1 - p_{turn}) \sigma_{fwd}^2} (1 - 2p_{flip})^q \quad (\text{A14})$$

This is the equation used to fit the data in **Figure 1H**.

An estimate of  $p_{flip}$  was calculated as follows. If only turns are considered :

805  
806  
807  
808  
809  
810  
811  
812  
813  
814  
815  
816  
817  
818  
819  
820  
821  
822  
823  
824  
825  
826  
827  
828  
829  
830  
831  
832  
833  
834  
835  
836  
837  
838  
839  
840

841  
842  
843  
844  
845  
846  
847  
848  
849  
850  
851  
852  
853  
854  
855  
856  
857  
858  
859  
860  
861  
862  
863  
864  
865  
866  
867  
868  
869

$$\begin{aligned} \langle \delta\alpha_n \delta\alpha_{n+1} \rangle &= p_{turn}(1 - p_{flip}) \langle |\delta\alpha_n| |\delta\alpha_{n+1}| \rangle - p_{turn} p_{flip} \langle |\delta\alpha_n| |\delta\alpha_{n+1}| \rangle \\ &= p_{turn}^2 [(1 - 2p_{flip}) \langle |\delta\alpha_n| |\delta\alpha_{n+1}| \rangle] \end{aligned}$$

thus :

$$\frac{\langle \delta\alpha_n \delta\alpha_{n+1} \rangle}{\langle |\delta\alpha_n| |\delta\alpha_{n+1}| \rangle} = p_{turn}^2 [(1 - 2p_{flip})] = C_1$$

And finally

$$p_{flip} = \frac{1}{2} \left( 1 - \frac{C_1}{p_{turn}^2} \right) \quad (2)$$

### Mean square reorientation (MSR)

The mean square reorientation for a lag  $q \in \mathbb{N}^*$  is defined by:

$$M_q = \langle (\alpha_{n+q} - \alpha_n)^2 \rangle \quad (A15)$$

and can be expressed as a sum of correlations as follows:

$$\begin{aligned} M_q &= \left\langle \left( \sum_{i=1}^q \delta\alpha_{n+i-1} \right)^2 \right\rangle \\ &= \left\langle \sum_{i=1}^q \sum_{j=1}^q \delta\alpha_{n+i-1} \delta\alpha_{n+j-1} \right\rangle \\ &= \sum_{i=1}^q \sum_{j=1}^q \langle \delta\alpha_{n+i-1} \delta\alpha_{n+j-1} \rangle \\ &= q \langle \delta\alpha_n^2 \rangle + \sum_{i=1}^q \sum_{\substack{j=1 \\ j \neq i}}^q \langle \delta\alpha_{n+i-1} \delta\alpha_{n+j-1} \rangle \\ &= q \langle \delta\alpha_n^2 \rangle + 2 \sum_{i=1}^{q-1} (q-i) \langle \delta\alpha_n \delta\alpha_{n+i} \rangle \\ &= \left[ q + 2 \sum_{i=1}^{q-1} (q-i) C_i \right] \langle \delta\alpha_n^2 \rangle \end{aligned}$$

and using equation A13 we finally obtain the expression used in **Figure 11**:

$$M_q = \left[ q + 2 \sum_{i=1}^{q-1} (q-i) C_i \right] \left( p_{turn} \sigma_{turn}^2 + (1 - p_{turn}) \sigma_{fwd}^2 \right) \quad (A16)$$

## 870 Appendix 2

### 871 Neuronal model of the ARTR

872 The architecture of the ARTR neuronal model is shown in **Figure 5A**. The circuit consists  
873 of two modules selective to lefward or rightward turning. Each module receives recurrent  
874 excitatory, cross-inhibitory and sensory inputs. The firing rates of the left/right ARTR modules  
875 are governed by two differential equations:

$$876 \left\{ \begin{array}{l} \tau \dot{r}_L = -r_L + \phi(w_E r_L - w_I r_R + I_0 + I_L(t)) + \epsilon(t) \\ \tau \dot{r}_R = -r_R + \phi(w_E r_R - w_I r_L + I_0 + I_R(t)) + \epsilon(t) \end{array} \right. \quad (A17)$$

877  $r_{L,R}$  stands for the firing rate of the left (resp. the right) neuron of the ARTR.  $w_E r_{L,R}$   
878 corresponds to the recurrent excitatory current in the left (resp. the right) part of the  
879 network.  $w_I r_{L,R}$  corresponds to the cross-inhibitory current coming from the contralateral  
880 side of the network.  $I_0$  is a constant,  $\epsilon$  a white noise. The function  $\phi$  is a non-negative spiking  
881 constraint such that  $\phi(x > 0) = x$ , whereas  $\phi(x < 0) = 0$ . We fix  $\tau = 100ms$ ,  $I_0 = 20A$  and  $\epsilon(t)$  is  
882 a white noise with standard deviation of 500.

883 And

$$884 \left\{ \begin{array}{l} I_L(t) = I_{light}(1 - c(t))/2 \\ I_R(t) = I_{light}(1 + c(t))/2 \end{array} \right. \quad (A18)$$

885 Where  $I_{light}$  is a constant,  $c(t)$  is the contrast seen by the fish.

886 In such a dynamical system, the self-excitation and the noise produce the rise and fall of  
887 activity in one population, while inhibition ensures that only one population can be active at  
888 a time. Qualitatively  $w_I$  controls the anticorrelation between left and right neuron activity.  
889 If  $w_I$  is too low the activity of each side of the network is independent. We fix  $w_I = 7A.s$   
890 such that the anticorrelation of the left and right signals is comparable to the one described  
891 in **Wolf et al. (2017)**: -0.4.  $w_E$  controls the ability for each side of the network to have a  
892 stable activity across time longer than  $\tau$ . Schematically, the dynamical system described  
893 by the **Equation A17** can have three different regimes given the values of  $w_E$ . One regime  
894 is characterized by an absence of stable activity (low  $w_E$ ). Another regime sees one of the  
895 neurons of the network active forever whereas the other is silent ( $w_E \sim 1$ ). The third regime  
896 displays an alternation of stable activity between each side of the network. The fixation  
897 time of the left or the right neuron is controlled by  $w_E$ . An intuitive metric for this fixation  
898 time is given by the shape of autocorrelation of  $r_{L,R}$ . We choose  $w_E$  such that the fits of the  
899 autocorrelation of  $r_L - r_R$  and the orientation correlation of turning bouts by an exponential  
900 decreasing function coincides (**Figure 5C** and **Figure 1J**). For the phototactic simulated activity,  
901 we modelled the effective visual contrast seen by the fish with a linear function of the angular  
902 distance between the fish and the light source.

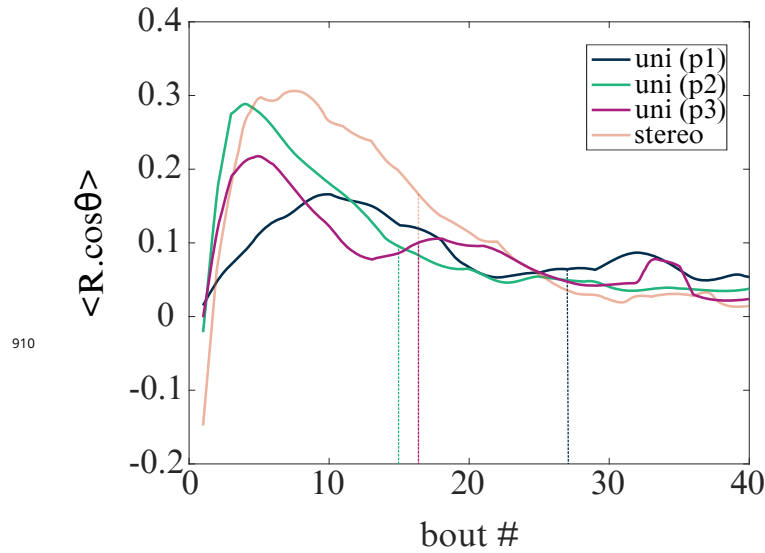


**Figure 2-Figure supplement 1.** Evolution of the mean resultant vector length  $R$  projected on the direction of the virtual light source in time (bout#) for the 4 tested phototactic modalities (uniform illumination : (p1-p3) and stereo-visual contrast). The vertical lines represent the median number of bouts per sequence in each modality.

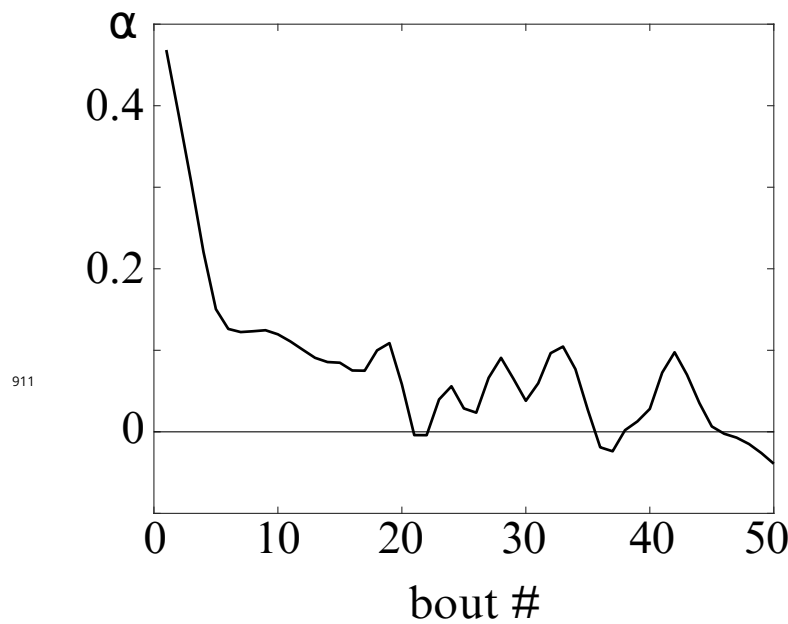


**Figure 2-Figure supplement 2.** Slope  $\alpha$  of  $\mu_{turn} = f(C)$ , representing the bias towards the brighter side, at different bout numbers. The bias quickly drops, this can be explained by the higher variance of  $\delta\theta$  during the first bouts of a sequence (change of illumination intensity) and then the selection of individuals which are not very responsive to the stimulus.

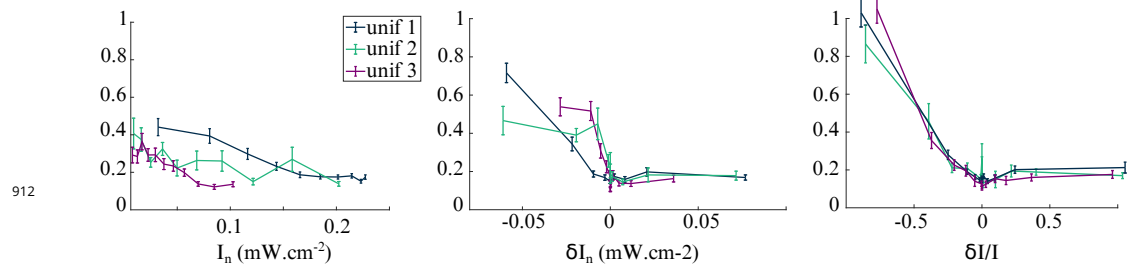


**Figure 3-Figure supplement 1.** Testing klinotaxis with spatially uniform illumination (orientational profiles p1-p3). Change in variance of  $\delta\theta$  at bout  $n$  for two different parameters : absolute intensity  $I_n$ , absolute change in intensity  $\delta I_n = I_n - I_{n-1}$  and relative change in intensity  $\delta I/I = 2 \frac{I_n - I_{n-1}}{I_n + I_{n-1}}$ .

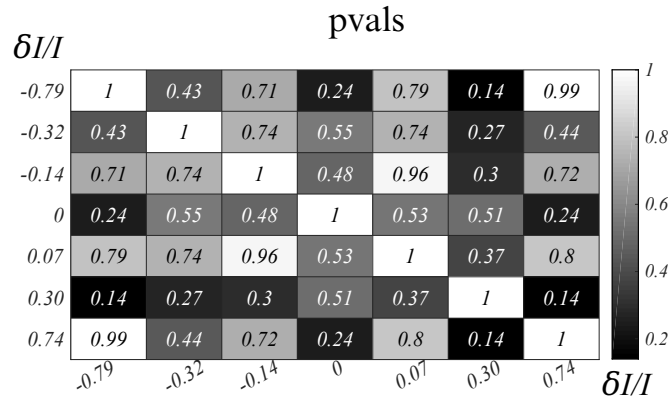
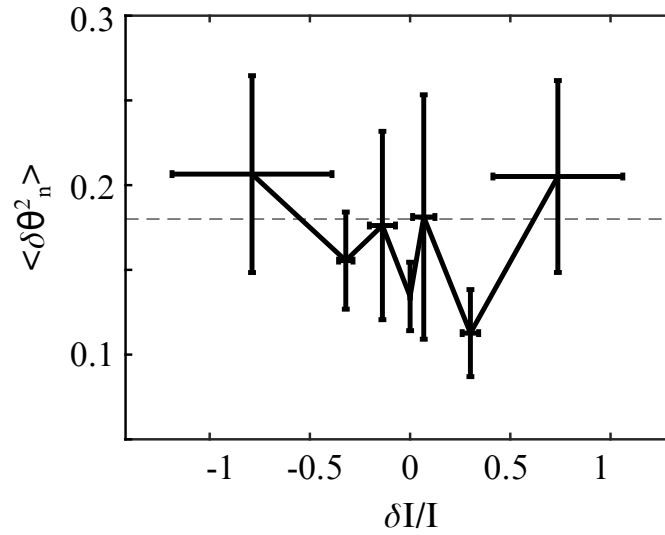


**Figure 3-Figure supplement 2.** Upper figure : Testing klinotaxis with spatially uniform illumination (orientational profile p2).  $N=12$  enucleated zebrafish larvae. No significant change in variance of  $\delta\theta$  upon decrease of relative difference of intensity. Neutral conditions of control larvae represented with gray dashes. Lower figure :  $p_{values}$  of two-sample t-tests of the distributions of  $\langle \delta\theta^2 \rangle$  in the different bins. None of the bins has a significantly different mean value from another.

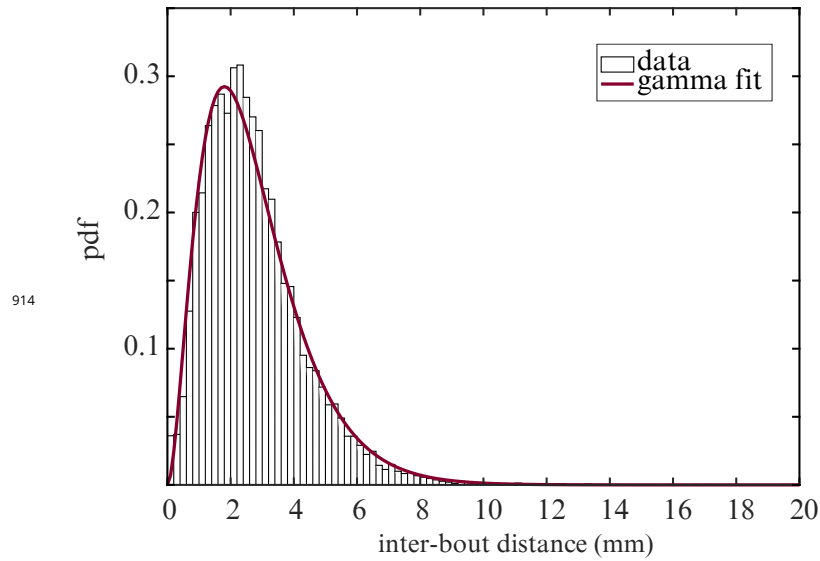


**Figure 5-Figure supplement 1.** Probability distribution function of the distance between two successive bouts. Fit : gamma distribution.

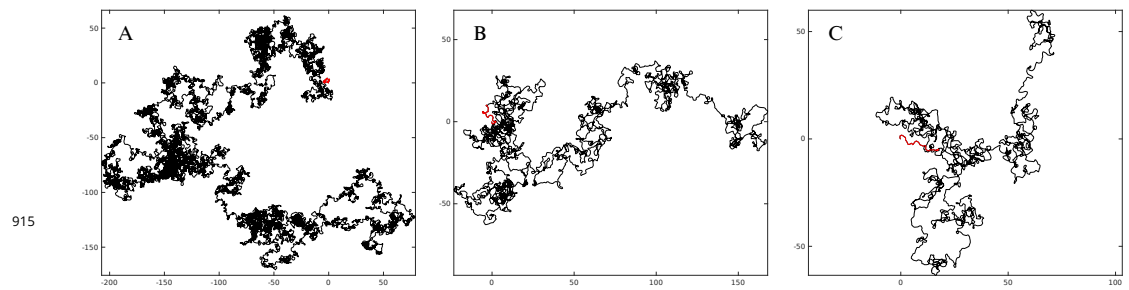


**Figure 5-Figure supplement 2.** Examples of simulated trajectories with different inter-bout intervals  $\tau_n = 1$  displaying different fractal dimensions  $H$ . Units : mm. (A)  $\tau_n = 1$  second,  $H = 1.5$ . (B)  $\tau_n = 5$  seconds,  $H = 1.3$  (C)  $\tau_n = 10$  seconds,  $H = 1.2$ . Red segments represent the onset of a sequence.